Textural studies of vesicles in volcanic rocks: An integrated methodology

Thomas Shea, Bruce F. Houghton, Lucia Gurioli, Katharine Cashman, Julia E. Hammer, Barbara J. Hobden

Textural studies of vesicles in volcanic rocks: An integrated methodology

Thomas Shea [a,*], Bruce F. Houghton [a], Lucia Gurioli [a,1], Katharine V. Cashman [b], Julia E. Hammer [a], Barbara J. Hobden [c]

[a] Department of Geology and Geophysics, SOEST, University of Hawaii, 96822, Honolulu, HI, USA
[b] Department of Geological Sciences, University of Oregon, 97403, Eugene, OR, USA
[c] Department of Earth Sciences, University of Waikato, Hamilton, PB3105, New Zealand

Vesicles in volcanic rocks are frozen records of degassing processes in magmas. For this reason, their sizes, spatial arrangements, numbers and shapes can be linked to physical processes that drive magma ascent and eruption. Although numerous techniques have been derived to describe vesicle textures, there is no standard approach for collecting, analyzing, and interpreting vesicular samples. Here we describe a methodology for techniques that encompass the entire data acquisition process, from sample collection to quantitative analysis of vesicle size and number. Carefully chosen samples from the lower, mean and higher density/vesicularity endmembers are characterized using image nesting strategies. We show that the texture of even microvesicular samples can be fully described using less than 20 images acquired at several magnifications to cover efficiently the range of existing vesicle sizes. A new program (FOAMS) was designed to perform the quantification stage, from vesicle measurement to distribution plots. Altogether, this approach allows substantial reduction of image acquisition and processing time, while preserving enough user control to ensure the validity of obtained results. We present three cameo investigations — on basaltic lava flows, scoria deposits and pumice layers — to show that this methodology can be used to quantify a wide range of vesicle textures, which preserve information on a wide range of eruptive conditions.

1. Introduction

Volcanologists use the textures of volcanic rocks to identify processes occurring before, during and immediately after eruption of magma (e.g., Sparks, 1978; Houghton and Wilson, 1989; Cashman and Mangan, 1994). Vesicles in pyroclasts and lava flows document processes of gas exsolution, expansion, and escape that drive most volcanic eruptions. Gas exsolution is controlled by magma decompression and consequent changes in volatile saturation conditions (e.g. Papale et al., 1998). The relative rates of bubble nucleation and growth control primary vesicle textures. Nucleation and growth rates are determined by both intensive magma properties (e.g. initial volatile content and melt viscosity) and extensive properties (e.g., magma ascent rate, fragmentation and quenching; these primary textures may be further modified by bubble deformation, coalescence, expansion, or gas escape (e.g. Sparks, 1978; Cashman and Mangan, 1994, Klug and Cashman, 1994; Toramaru, 1995; Simakin et al., 1999; Klug et al., 2002; Polacci et al., 2003; Gurioli et al., 2005; Allen, 2005; Piochi et al., 2005; Sable et al., 2006; Adams et al., 2006; Noguchi et al., 2006; Mastrolorenzo and Pappalardo, 2006; Lautze and Houghton 2007; Cigolini et al., 2008).

Quantification and interpretation of vesicles have been an important research topic in volcanology. However, diverse methodologies have been used to describe vesicle textures. As a result, comparisons between different studies have been hindered by differences in approaches to sampling and textural quantification. Here we present an efficient and accurate strategy for acquiring textural information from vesicular samples. We describe field sampling protocols, sample processing methods, and image acquisition and rectification techniques that employ a new Matlab-based program named "FOAMS" (Fast Object Acquisition and Measurement System). FOAMS allows calculation of parameters that describe the spatial arrangement, as well as the size and number of vesicles in volcanic samples. Key input parameters are evaluated and tested on three examples (Makapuu lava flow, Hawaii; scoria from Villarrica, Chile; and pumice from Vesuvius, Italy), where the methodology is applied to textural characterization of samples generated by very diverse eruption styles.

2. Background

The following sections summarize the different approaches to characterizing textures in volcanic rocks and the ways in which they are commonly represented graphically.

* Corresponding author. Tel.: +1 808 956 8558.
E-mail address: tshea@hawaii.edu (T. Shea).
[1] Current address: Laboratoire Magmas et Volcans, Universite Clermont-Ferrand II, 63000, France.

2.1. The 3D approach: X-ray microtomography

In recent years, X-ray microtomography (XRCMT) has been increasingly applied to texture characterization in volcanic rocks. This technique allows the imaging of tens to hundreds of slices through a rock sample in a relatively short time interval. The obtained 2D slices are then merged to create a 3D representation of the sample. While Ketcham and Carlson (2001) and Ketcham (2005) introduced the many uses of XRCMT in geology, Proussevitch et al. (1998) were the first to apply XRCMT to vesicles in Hawaiian basalts. Only recently the technique has been merely widely applied, as Song et al. (2001) examined basaltic scoria and Polacci et al. (2006, 2009) studied scoria and pumice samples from Stromboli, Villarrica and the Campanian Ignimbrite. Polacci et al. (2008, 2009) also provided an example of how connectivity as measured by tomography can be used to infer outgassing during ascent of Strombolian magmas. Okumura et al. (2006, 2008) exploited the ability of XRCMT to successfully measure vesicles that may be significantly deformed by shearing, and derived permeability values for rhyolitic magmas under various stress conditions. Currently, XRCMT is possibly the only viable technique to study sheared and deformed samples adequately, especially in terms of measuring key parameters such as permeability (e.g., Wright et al., 2006). Unfortunately, the technique is still not able to resolve very thin glass walls present in pumice (Song et al., 2001; Bai et al., 2008), and typically, smallest measured objects are within the range of 10–70 μm (Gualda and Rivers, 2006; Proussevitch et al., 2007b, Degruyter et al., 2010), which is acceptable for basaltic lavas and some scoria samples but not for pumice. Thin glass walls can be lost during imaging, and unconnected objects merged. This in turn increases apparent permeability and vesicle interconnectivity (Song et al., 2001), and causes discrepancies in vesicle number densities (N_V, mm^{-3}): for instance, Polacci et al. (2006) found N_V in the range of 10^3–10^4 mm^{-3}, about an order of magnitude smaller than values that were measured in these samples by 2D imaging and conversion to 3D (Polacci et al., 2003). In addition, reconstruction of broken or missing glass walls is much more challenging in 3D and requires automated wall reconnection routines (e.g. Shin et al., 2005) with the assumptions they entail that cannot offer the same amount of user control that in the context of 2D. Thus, while XRCMT techniques are improving and are able to resolve smaller and smaller objects, there is still a need for other robust textural characterization methods that are applicable to all sample types, from vesicle-poor lava flows to pumice and reticulite.

2.2. The 2D approach: stereology

Studying textures in thin sections creates 2D data that ignores how particles are configured in the third dimension. Because sections through polydisperse objects are not likely to be cut routinely through their largest area (cut-effect), and since smaller objects have a lower probability of being intersected than larger ones (intersection probability), raw data from 2D images have inherent flaws. The assumption that cross-sections through particles can be used to quantify size and distribution is all the more erroneous when particles are elongate. To correct for these problems, statistical techniques to convert 2D areas into equivalent volumes were formulated early on and applied to particulate materials (e.g. Saltikov, 1967; Underwood, 1970). More recently, substantial progress has been made towards building models which account for intersection probabilities, cut-effects and variations in shape (e.g. Sahagian and Proussevitch, 1998; Higgins, 2000; Mock and Jerram, 2005; Morgan and Jerram, 2006).

In the methodology presented herein, the conversion method of Sahagian and Proussevitch (1998) is used to generate corrected vesicle size and number distributions. Their technique consists of calculating the number density of objects in given size classes (1 to i) per unit volume (N_V in mm^{-3}) by successive iterations of the number density of larger objects (N_{V1}, N_{V2}, N_{V3}, …N_{Vi}) assuming spherical geometry. The main advantages of this approach are that it is fast and does not require extensive computation. Geometric binning is employed instead of linear binning since it is more adequate for particle sizes that are distributed over several orders of magnitude. Geometric bins allow for a much better representation of the smaller size populations, which tend not to be resolved by linear bins (Proussevitch et al., 2007a).

A major issue with this method is that it does not account for elongate shapes, since cross-section probabilities for elongate objects cannot be expressed analytically. On the other hand, assuming a given aspect ratio for vesicles implies that some process has caused them to deform uniformly (i.e. deformation is constant throughout the sample). This is the major reason why this methodology cannot be easily applied to rocks whose vesicles are intensely sheared (e.g. fibrous or tubular pumice). For the study of pyroclasts that suffered little to no shearing or did not preserve shearing textures, the spherical assumption often holds true since bubble relaxation inherently favors equal distribution of stresses at the bubble–melt interface (Rust et al., 2003). In pumice, vesicles frequently show no preferential direction of elongation or a unique aspect ratio applicable to the entire population and, though spheres may poorly define these vesicles, a set of ellipsoids with defined aspect ratios may be less accurate.

2.3. Texture representation

Because each type of distribution plot possesses its own advantages and caveats, they are all displayed and compared whenever possible. Four types of distribution plots, along with visual (i.e. texture imaging), quantitative (i.e. computation of vesicularity, total vesicle number density, and modal/mean size) and, to a lesser extent, shape data, form the end-products of the methodology presented in this contribution.

Vesicle size and number analysis: during magmatic ascent, bubbles in magma nucleate and grow as volatiles are exsolved. The final number density and size distribution of bubble populations in a volcanic rock erupted at the surface depends not only on the available volatile concentrations, but also on the ability for this volatile phase to diffuse through the melt as well as the time available for expansion (i.e., time spent by magma in the conduit and/or at the surface) (Toramaru, 1995; Lyakhovsky et al., 1996; Proussevitch and Sahagian, 1996). Hence, investigating vesicle sizes and numbers can prove invaluable to characterize storage, ascent and eruption conditions (e.g. Klug and Cashman, 1994). Vesicle number densities per volume N_V (or per melt volume N_{Vcorr} when corrected for vesicularity and pre-vesiculation crystals) are typically higher in explosive eruptions than in effusive eruptions (Toramaru, 1990; Cashman and Mangan, 1994; Toramaru, 1995; Mangan and Cashman, 1996; Polacci et al., 2001; Sable et al., 2006). A tendency of N_V to increase with eruption intensity has been experimentally and numerically linked to the dependence of N_V on decompression rate, and on other properties such as diffusivity, viscosity and surface tension (Mangan and Sisson, 2000; Mourtada-Bonnefoi and Laporte, 2002, 2004; Lensky et al., 2004; Namiki and Manga, 2006, Toramaru, 2006; Cluzel et al., 2008) . Hence, N_V is expected to scale with SiO_2 content (e.g., Sable et al., 2006) and physical eruption parameters such as magma discharge rate or column height (e.g., Gurioli et al., 2008). As a consequence, obtaining accurate measurements of both vesicle size and number is crucial if valid physical comparisons are to be made between different eruptions.

Because vesicles vary significantly both in size and in number, textural data are always displayed as distributions. The four most recurrent plots in the size distribution literature are used either to display vesicle volume information (vesicle volume distributions VVD and cumulative volume distributions CVVD), or number of vesicles

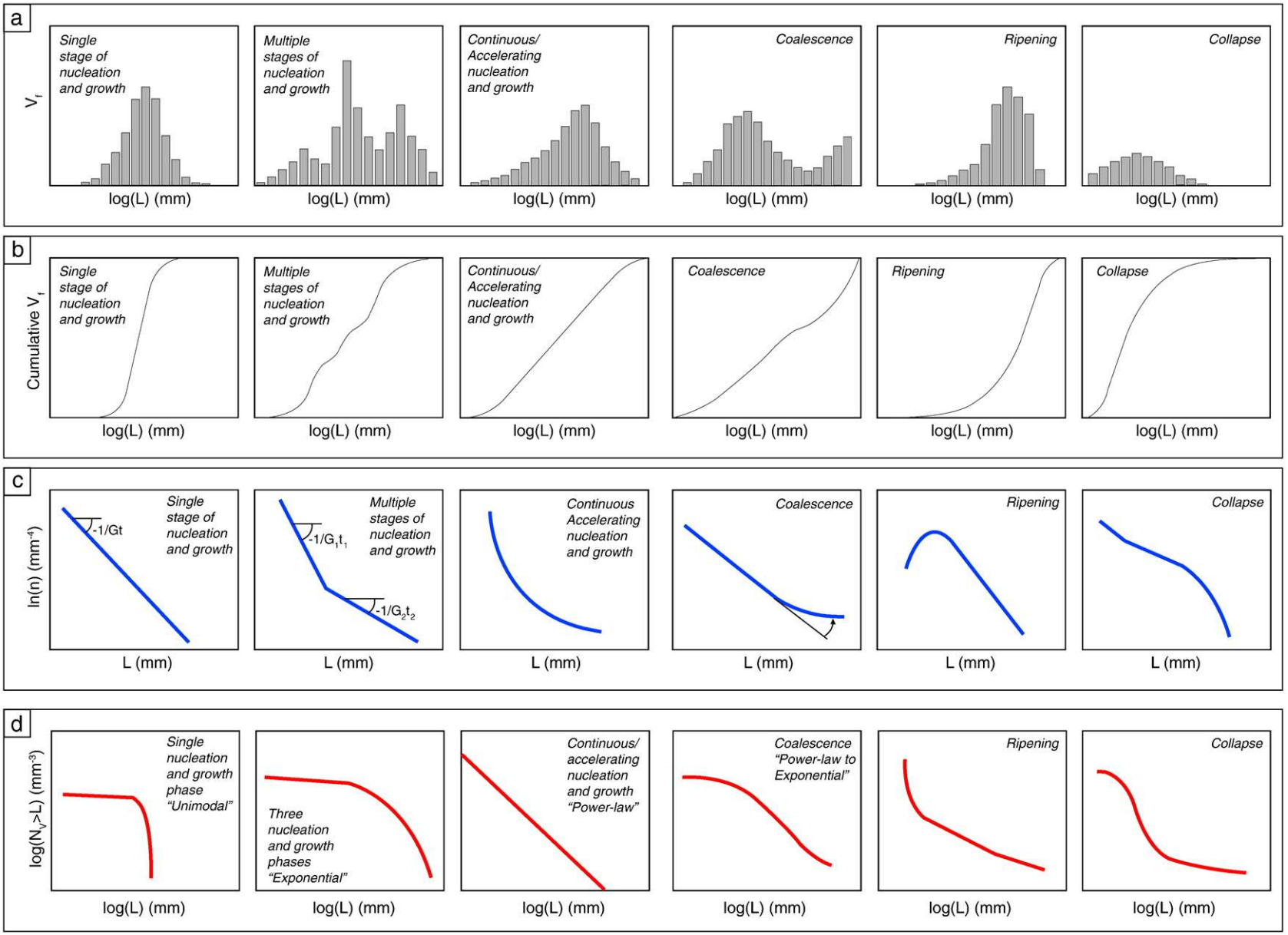

Fig. 1. Various ways to display textural characteristics through size (L) and number density (n or N_V) plots, and processes that they may be associated with (single or few nucleation events, multiple nucleation and growth events, continuous nucleation and growth, coalescence, ripening, and collapse, see text for explanation). (a) Simple volume fraction (V_f) size distribution (VVD), (b) cumulative volume fraction size distribution. (CVVD), (c) vesicle size distributions (VSD) in terms of number density n, and (d) cumulative number density plots $\log(N_V{>}L)$ vs. $\log(L)$ (CVSD). Because during magmatic ascent multiple vesiculation and degassing processes may occur simultaneously and overprint each other, such plots call for interpretative prudence. G is growth rate and t is time.

per class size information (vesicle size distribution VSD and cumulative size distributions CVSD). Fig. 1 displays examples of the four categories, as well as examples of the processes that may contribute to generating or modifying them.

VVDs are generally used to infer the nature of nucleation and/or coalescence events during the vesiculation history of pyroclasts (Fig. 1a) (e.g. Klug and Cashman, 1994). Typically, each mode is interpreted to illustrate a distinct pulse of nucleation and growth (Klug et al., 2002; Polacci et al., 2003; Lautze and Houghton, 2007); coalescence tends to skew the data positively or even produce a distinct larger mode (Adams et al., 2006; Gurioli et al., 2008), ripening produces a negative skewness (Mangan and Cashman, 1996), and bubble collapse dramatically reduces total vesicle volume fraction and modal size (Burgisser and Gardner, 2005; Sable et al., 2006).

CVVD plots are complementary to VVD as they provide essential knowledge about the contribution of each size range to the total vesicularity (Fig. 1b). A unimodal distribution produces a sigmoid-shaped curve, multiple modes add bulges to the curve (), coalescence tends to reduce the slope of the upper portions of the sigmoid, ripening shifts the curve to the right and accentuates the lower portion of the curve, while collapse likely will result in a curve shifted towards smaller sizes, with lessened contribution of large vesicles (Klug et al., 2002, Adams et al., 2006, Mongrain et al., 2008). Apart from basic statistics such as modes, means and standard deviations, no true quantitative data can be extracted directly from VVD or CVVD plots.

VSDs (or $\ln(n)$ vs. L plots, with L equivalent diameter in mm) are used commonly to infer kinematics of nucleation density and growth rate of crystals or bubbles (e.g. Marsh, 1988, 1998). According to Mangan and Cashman (1996), linear distributions denote steady-state nucleation and growth while an upward inflexion towards smaller sizes reflects ripening processes and a downward inflexion towards larger objects may be caused by coalescence (Fig. 1c). In turn, bubble collapse may produce a curve that plunges rapidly in the larger size classes. Hypothetically, if the data within a VSD plot follows a linear trend, growth rates (G, mm s^{-1}) can be determined from the slope of the curve and initial number density (n_0, mm^{-3}) calculated from the intercept at $L=0$, providing that some constraint exists on the timescale for nucleation and growth (τ). From the latter parameters, it is then possible to obtain nucleation rates (J, $mm^{-3}\ s^{-1}$). If no time constraint exists, only the total vesicle number density (N_{tot} in Mangan and Cashman, 1996; written N_{Vfit} herein to describe better its origin) and dominant diameter L_{Vfit} can be derived from the slope (see Appendix B for a brief summary of formulations).

CVSDs (or $\log(N_V{>}L)$ vs. $\log(L)$ plots) make use of population number density, and consider the number of objects per cubic mm with diameter greater than L. Gaonac'h et al. (1996a,b, 2005) and Blower et al. (2001, 2002) developed the idea that power-law distributions could better accommodate certain types of vesicle size distributions produced by continuous/accelerating nucleation (i.e. data generating curves on VSD plots). Possible curve trends associated with various processes are illustrated in Fig. 1d, and important formulations are reported in Appendix B.

Vesicle shape analysis has two major functions: first, it may provide information about the sphericity of objects (which in turn serves to validate or refute the assumption used for stereological conversion) and the geometry of the bubble–melt interface (i.e., whether vesicle walls form a simple sphere/ellipsoid or whether their interfaces are complex). Several factors control whether bubbles will be preserved as spheres within a given sample, related to the timescale available for relaxation (e.g. Namiki and Manga, 2006). Providing bubbles have insufficient time to relax and minimize their surface energy, simple or pure shear may cause vesicles to be elongated (Hon et al., 1994, Rust et al., 2003), and coalescence may produce complex polylobate shapes (Klug et al., 2002; Polacci et al., 2003). Bubble collapse (Adams et al., 2006; Mongrain et al., 2008) and significant groundmass crystallization (Klug and Cashman, 1994; Sable et al., 2006) result in increasing interface complexity. Hence to fully characterize vesicle shape within volcanic rocks, two main parameters are needed: a "roundness" parameter that determines whether the vesicle has a shape closer to a circle or an ellipse, and a "complexity" parameter that measures the tortuosity of vesicle outline (Appendix C).

3. Methods

The leitmotiv behind proposing a standardized methodology lies in improving the possibilities of comparing datasets from various eruptive settings. To ensure that the textural data that is being used to infer eruptive processes is robust, sampling and sample processing need to be approached rigorously. The following paragraphs contain suggestions for field sampling, vesicularity/density determination, sample imaging (strategies of image acquisition and rectification), as well as brief description of the stereological conversion technique utilized herein.

3.1. Field sampling

Two types of samples are generally collected from the field in physical volcanology: pyroclasts such as pumice, scoria, volcanic bombs, reticulite, or Pele's hairs and tears, and more competent rocks from welded falls or pyroclastic density current deposits (PDC), lava flows, dykes and domes emplaced effusively.

Sampling of pyroclasts (fall, PDC, or ballistics) is typically conducted at well constrained proximal sites, once the physical and chemical characteristics pertaining to the eruptive layer and their spatial variations have been thoroughly investigated. For impulsive discrete explosions (Vulcanian and Strombolian explosions) clasts are collected from the deposits of single explosions (e.g. Lautze and Houghton, 2007; Gurioli et al., 2008). For pumice and small scoria from more prolonged Hawaiian through Plinian explosions, over 100 juvenile clasts of diameter 16–32 mm are collected over a narrow portion of the stratigraphic unit (Houghton and Wilson, 1989; Gurioli et al., 2005). Where the juvenile clasts within a deposit are unusually diverse the sample size is increased to more than 200 clasts to adequately categorize the endmember textures (Polacci et al., 2003). Such a large number of clasts within the eruptive unit ensure that both the low and high end of the vesicularity range are adequately sampled (Houghton and Wilson, 1989). In the case of a fallout deposits, typically a stratigraphic range of 1–3 clast diameters in thickness is selected to minimize the eruption interval that is sampled. Larger pyroclasts such as bombs are sampled individually to look for significant textural variations from core to rim, thus several thin sections are preferably made from different internal domains within each bomb (e.g. Wright et al., 2007).

When more competent eruptive units such as lava flows (e.g. Cashman et al., 1994), welded pyroclastic deposits (e.g. Carey et al., 2008), dykes/sills or domes are sampled, several portions are usually broken from or cored through the unit in order to capture textural variations. In the case of competent rocks, it is recommended to take samples as large as 20 cm in diameter, small enough to be scanned. At even larger scales, Polacci and Papale (1997) illustrated that textural quantification can be achieved within meter-sized outcrops using reconstructive photography in the field.

3.2. Density/vesicularity measurements, thin sections

Prior to performing density measurements, collected samples are cleaned and dried at $T>100$ °C for 24 h. For pumice or scoria samples, a subset of clasts is usually ranked by decreasing size and numbered from 1–100 (Fig. 2). For other specimens, especially large ones, the rock is cut into halves, one half being kept for scanner imaging and the

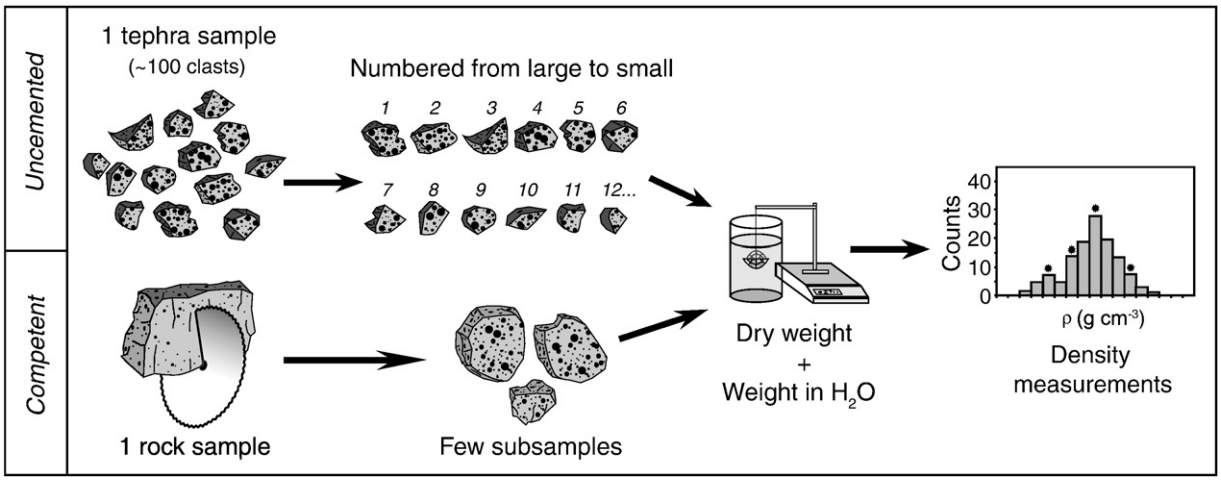

Fig. 2. Illustrative cartoon of sampling procedure and density measurements.

other serving for density measurements and microscopic imaging. Within the half serving for density, several subsamples corresponding to distinct textural units are carefully removed (Fig. 2). If the sample is homogeneous to begin with, no further subdivision is required, provided that its size is large enough for weighing in the laboratory.

The density measurement methods described here are derived from Houghton and Wilson (1989). Clasts or sample subsets are weighed in air (mass ω_{AIR} in g), and either individually wrapped into polyethylene film (of wet weight ω^{film}_{WATER}), or made impermeable using water-proofing spray. They are then weighed once more immersed within water (ω_{WATER}). Specific gravity, and thereby density is expressed as:

$$\rho_{BULK} = \frac{\omega_{AIR}}{\omega_{AIR} - (\omega_{WATER} - \omega^{film}_{WATER})} \quad (1)$$

For buoyant particles, e.g., pumice, the clasts are forced down using a ballast of known wet weight and volume.

Finally, the dense rock equivalent (DRE) density of the magma is used to obtain porosity (ϕ) or vesicularity ($\phi \times 100$):

$$\phi = \frac{\rho_{DRE} - \rho_{BULK}}{\rho_{DRE}} \quad (2)$$

This technique is rapid and yields large arrays of data. Other alternatives include measuring density/porosity directly using a He-pycnometer, yielding both connected and isolated vesicle fractions (Rust and Cashman, 2004). For pumice and scoria sample datasets, density is plotted on a histogram to choose only a few clasts that represent the different endmembers from the entire distribution (Fig. 2). In this manner, 3 to 8 clasts are typically chosen to represent low (1 to 2 clasts), modal (1 to 4 clasts) and high (1 to 2 clasts) vesicularities. For larger samples from lava flows, domes and bombs, tephra clasts showing substantial internal variability, density/vesicularity measurements are done on the subsamples prepared for each textural zone. The chosen clasts/subsamples are made into thin sections with, in the case of pumice or reticulite, impregnation with resin to avoid breakage of thin glass walls.

3.3. Image acquisition

The largest vesicle populations can be imaged adequately by a scanner, either using a thin section or the sectioned sample itself. For thin sections, scanners possessing slide illumination functions allow better resolution. Larger magnifications (i.e. higher than 25×) are best mapped through Scanning Electron Microscopy (SEM), in back-scattered electron imaging (BSEI) mode, using chemical contrasts between phases. Before thin sections are carbon coated, it is practical to outline and highlight phenocrysts present on the scanned image, since their proportions are needed for number density corrections. In cases where the sample is very phenocryst-rich, thin sections can be scanned between two polarized foils, cut perpendicular to each other. This technique allows the operator to observe crystals in distinctive colors, as in an optical microscope (Pioli et al., 2007). The SEM working distance must be set higher for lower magnifications (e.g. 45–50 mm for 25× on a JEOL-5900 SEM) and lower for higher magnifications (e.g. 15–20 mm for >75×), and contrast/brightness adjusted to obtain the best representation of bubbles and different crystals present in the matrix. This facilitates image processing into inputs for the FOAMS program. Details on additional SEM imaging techniques (e.g. X-ray mapping) can be found in Blundy and Cashman (2008).

3.4. Choice of magnifications

Vesicles in volcanic rocks are typically polydisperse, with sizes that range from microns to centimeters; a single clast may contain vesicles varying in size by 4–5 orders of magnitude (Klug et al., 2002). Characterizing this range of vesicle sizes requires image acquisition over a similar range of scale (e.g., Gurioli et al., 2005; Sable et al., 2006; Adams et al., 2006; Lautze and Houghton, 2007). Accurate size data (either 2D or 3D) requires a statistically significant number of vesicles to be measured within each size range; this, in turn, requires definition of both the range of magnification needed to cover the range of vesicle sizes, and the minimum number of images per magnification required to sample each size range adequately.

The magnification range is determined by identifying the smallest and largest vesicles within the sample. For the lowest magnification, we use an area that is 1–2 orders of magnitude larger than the largest vesicle. When vesicles are ≤5 mm, a thin section suffices; when vesicles exceed this size, it may be necessary to scan either a rock slab or multiple thin sections. Similarly, the highest magnification has to record the smallest vesicles at a resolution that is sufficient to represent individual vesicles. Fig. 3a shows the minimum number of pixels (in area or equivalent diameter) required to represent an object and the uncertainties associated with any pixel imaging error. For instance, in a 10-pixel diameter object (~80 pixels in area), misrepresentation of 1 pixel will cause a 1.3% error in the measurement. Alternatively, one imperfectly imaged pixel in an object measuring 5 pixels in diameter (~20 pixels in area) will result in a 5% error. Fig. 3b illustrates the errors associated with the choice of minimum equivalent diameter (in μm) for a range of magnifications. The plot is

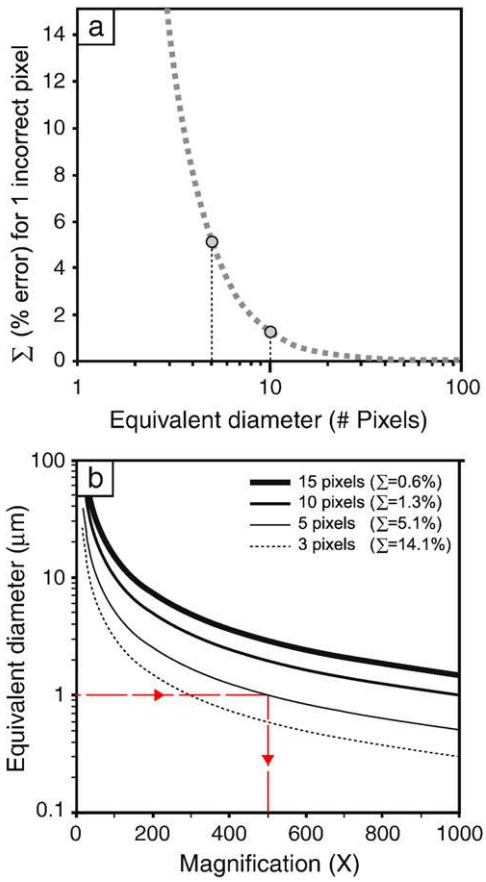

Fig. 3. Resolution and magnification within imaging techniques. (a) Influence of minimum diameter. The dashed gray curve illustrates the error Σ (right *y*-axis) associated with misrepresentation of 1 pixel in area within a vesicle. (b) Minimum vesicle diameter measurable for various magnifications. If vesicles as small as 1 µm in diameter are present within the sample and need to be imaged, maximum magnifications of 500× are sufficient assuming a resolution of 5 pixels minimum per vesicle (arrowed dashed line).

used as follows: through preliminary observation (SEM or petrographic microscope), an estimate of the minimum vesicle size within samples is made. In Fig. 3b, if a 1 µm-large equivalent diameter was adequately represented by 7 pixels in area (3 pixels equivalent diameter) a maximum magnification of around 300× could be used. The uncertainty associated with one misrepresented pixel is however very high (~14%), resulting in large errors in the size distribution. A better alternative is to have a minimum area of either 80 pixels (10 pixel equivalent diameter) to ensure ~1% error or 20 pixels if the researcher accepts a larger 5% error, and choose the corresponding maximum magnification at 500×. The purpose of this choice is to ensure that the smallest vesicles are imaged adequately while minimizing the number of images to process. Very high magnifications will result in better resolutions but require many images to enclose the same number of the smallest vesicles. As we argue in the following section, a minimum of 10 of the smallest vesicles needs to be measured at the highest magnification (excluding edge vesicles) to define the size threshold and maximum magnification used. Intermediate magnifications should be chosen so that substantial vesicle size overlap occurs between each set of magnifications.

3.5. Imaging strategy

As the area encompassed by a single image scales inversely with its magnification, the number of images needed to capture heterogeneities increases with decreasing feature size. To determine the sensitivity of the vesicle size data to the sampling strategy used, we compare data from: a 73-image grid strategy (one thin section, 24 images at each of three magnifications), a 25-image grid strategy (one thin section, 8 images at each of three magnifications), and a 15-image nest strategy (one thin section, increasing number of images at each of three magnifications) (Fig. 4). The grid strategy is similar to point counting and ensures that areas are sampled irrespective of the operator decision-making process. However, this strategy is time-consuming and may result in sampling areas containing few or no small objects. Less time-consuming approaches include imaging 8 frames instead of 24 at each magnification (25-image nest strategy, Fig. 4b) or increasing the number of images with magnification (15-image nest strategy, Fig. 4c). These user-defined methods have the advantage of saving time but place the burden of assessing textural heterogeneity with the operator, thus introducing potential for operator-induced bias. We introduce the term Image Magnification Ratio (IMR) to designate the number of images acquired within each subsequent nest. In all grid techniques, IMR = 1:1, whereas in the nested strategy, IMR > 1:1. The choice of IMR values does not need to remain constant throughout the series of nests; it should promote both minimization of number of images to 20 or less as well as preservation of enough surface area to adequately represent each vesicle size range.

To test the relative accuracy of the three strategies, we compare the measured number density of vesicles (N_A, mm^{-2}) in a pumice sample with a wide vesicle size range that required four different magnifications. Largest vesicles were around 5 mm, thus the lowest magnification was chosen at 5× (entire thin section). Smallest vesicles measured about 5 µm, hence the largest magnification needed was around 250× (Fig. 3). Intermediate magnifications were 25× and 100× to allow sufficient size overlap between images. Fig. 5 shows that the 72-image and 25-image grid techniques produce fairly smooth decreases in number density with increasing vesicle size. Number density data from the 15-image nest are somewhat noisier but still allow adequate characterization of size distributions. From

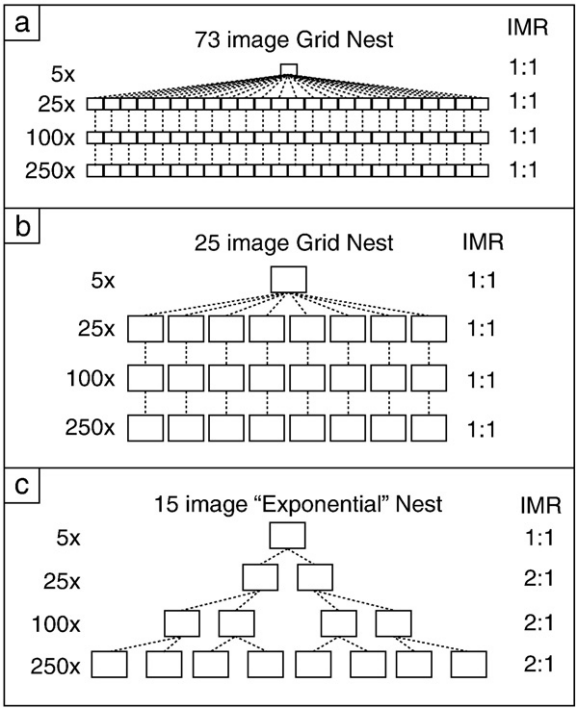

Fig. 4. The three tested imaging strategies; (a) a 73-image grid nest, with one image randomly chosen within the previous magnification, (b) a 25-image grid nest of similar configuration, and (c) an example of exponential nesting, where each magnification possesses twice as many images than the previous one and chosen nests are not randomly located within each magnification. IMR: Image Magnification Ratio.

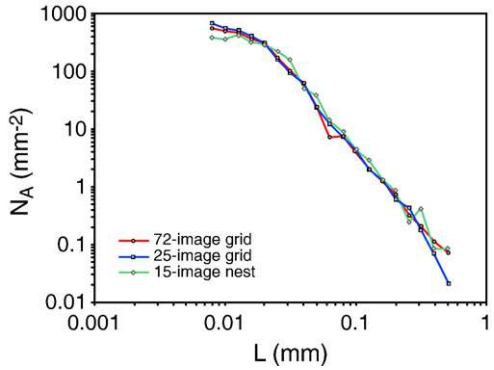

Fig. 5. Number of objects per melt area for different size classes measured within pumice samples from Taupo for each of the three imaging strategies. Note the good overall correspondence between the obtained curves which allows reducing the number of images required to adequately represent the sample overall.

this simple comparison between imaging strategies, we calculate that for a 15-image nest to adequately represent the small vesicle population (i.e. for the 15-image and the 72-image strategies to have indistinguishable N_A vs. L curves at $L<0.05$ mm), a minimum of 10 vesicles per image at the largest magnification must be counted (here 80 vesicles minimum for 8 images at 250×). The actual number of images used in any given nesting strategy depends on the vesicle size range and the sample heterogeneity. If both very small and very large vesicles are present and the sample displays substantial textural variations, then additional series of images are usually captured. Conversely, when samples are homogeneous and characterized by a narrow size range, fewer image nests are needed.

3.6. Image rectification

To reduce the amount of time spent performing these corrections, a detailed methodology that provides step-by-step guidelines on how to standardize and accelerate image rectification using readily available software is made available (http://www2.hawaii.edu/~tshea). Several factors are responsible for making image rectification time-consuming: first, vesicle walls in pumice or scoria clasts are often thin and may not be entirely resolved by the imaging instrument. Moreover, such walls can be destroyed as thin sections are made, and may end up as fragments within vesicles (Fig. 6a). Thus, broken walls need to be reconnected and loose fragments have to be deleted from the vesicle area. Secondly, cross-sections that have a 3D-like texture when viewed through the SEM (Fig. 6b) also require corrections. Lastly, and most importantly, imaged features (glass, vesicles, and crystals) never have truly homogeneous grayscale levels but show a spectrum of shades. Since FOAMS identifies objects based on their grayscale level, all counted features of a given type have to have uniform grayscale values (Fig. 6c). The amount of time spent preparing images will depend on the quality of the thin section, the fragility of the sample, the quality of the images (i.e. instrument), and on the number of magnifications needed to cover all vesicle size ranges.

3.7. Stereological conversion and binning

Although the reader is directed to Sahagian and Proussevitch (1998) for complete details concerning this procedure, the stereological formulations used here are summarized in Appendix A. Their method consists in deriving N_{Vi}, the number density of objects of size i per unit volume from N_{Ai}, the number density per unit area via an expression of the probability of intersecting spheres of given sizes through their maximum cross-sectional area P_i. To obtain N_{Vi} from N_{Ai} (Appendix A), Underwood (1970) introduced a useful parameter called the mean projected height ($\overline{H}_i'$, mm), which represents the mean distance between parallel planes tangential to the object boundary. For spherical particles, this equates to the characteristic diameter of each size class (L, mm). The diameter is thus used to correct N_A values for intersection probabilities on the basis of the stereological assumption $N_V = \frac{N_A}{L}$ (Underwood, 1970), and then corrected for the cut-effect (see

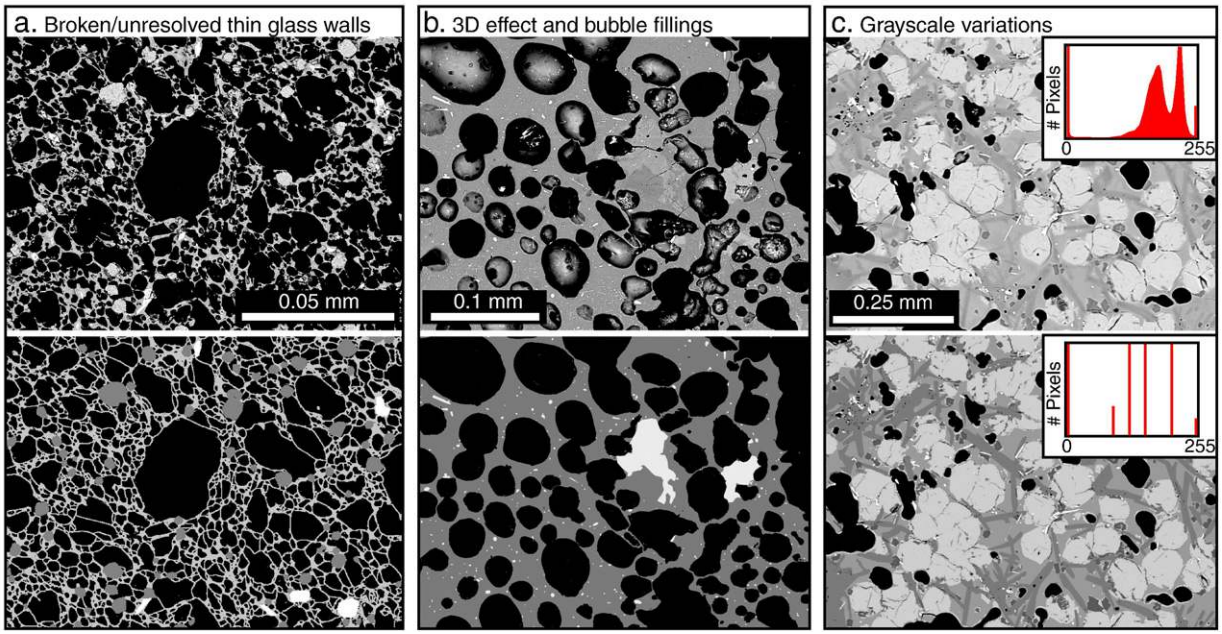

Fig. 6. Common issues with SEM images obtained from thin sections (top), and grayscale image resulting from repairing and processing each image (bottom). (a) Vesuvius 79AD EU2 sample showing a significant amount of broken glass walls as well as extremely thin ones. (b) 3D effect caused by intersecting small objects within a somewhat thick section, and broken glass and crystal fillings within some vesicles. (c) Illustration of problems of heterogeneous grayscale variations within raw SEM images (top histogram), and conversion to homogenous grayscale levels after image processing (bottom histogram). For guidelines to avoid grayscale conversion issues, see manual in online additional material.

Appendix A) to calculate final number densities (N_{Vi}, mm^{-3}), and the volumes of equivalent spheres (V_i, mm^3). N_{Vi} and V_i are used subsequently to determine volume fraction for each class (Vf_i):

$$Vf_i = N_{Vi} V_i \quad (3)$$

Volume fractions derived from the sum of converted N_{Vi}'s are generally less reliable than those one may obtain through direct measurements of vesicularity since the former relies on the assumption of perfect sphericity for each vesicle. To correct for this, Vf_i is normalized to the measured bulk vesicularity of the clast.

Depending on whether bubble growth occurred prior to, during, or after formation of crystal phases in the melt, a number density correction may be needed ("melt-referenced N_V"). A second correction is needed to allow for the volume taken up by the vesicles themselves (e.g. Klug et al. 2002). To obtain N_V corrected for vesicularity (N_{Vcorr}), number density is divided by $(1-\phi)$. Both crystal and vesicularity corrections are particularly useful if one aims to investigate the actual number of bubbles that nucleated within the melt (Proussevitch et al., 2007a).

3.8. Magnification cutoffs

Overlapping size bins for adjacent magnifications ensures that all vesicle sizes are adequately represented. We illustrate a method of merging data from different magnification images using an example of pumice from Vesuvius (79AD eruption, white magma, EU2 unit; Gurioli et al., 2005). Pumice clasts contain vesicles of sizes varying between 0.001 and about 4 mm. Four magnifications are chosen to cover this extensive size range, thus four N_A vs. L curves must be merged to generate the final size distribution (Fig. 7a). However, the transition from magnification 2 to 3 is slightly user-biased because most small vesicles were discarded from the second magnification. We have tested three different methods for merging these data. First, we applied arbitrary cutoffs at each new order of magnitude ("Magnitude jumps", Fig. 7b). The resulting size distribution is very irregular, with several apparent modes and sharp jumps between size bins. Second, we imposed a transition that minimized slope differences in the curves ("Minimized slope" in Fig. 7b), an approach that produced a smoother obtained distribution and fewer apparent modes than the first approach. Finally, we defined the shift to minimize the change in N_A values at the shift from one curve to another ("Minimized ΔN_A" in Fig. 7b). This generates smooth size distributions with 2 modes and no sharp bin transitions (Fig. 7b and c). This simple example illustrates the importance of using care when merging data across many image magnifications. The comparison between calculated N_V data shows that values are rather insensible to merging practices so as long as the smallest (and most numerous) vesicle population is well represented.

4. FOAMS: program structure and mode of operation

4.1. Overview

FOAMS is a Matlab™-based program designed to facilitate the measurement and stereological conversion of objects within a set of one to twenty images. All the details on the program's structure are available on the web (http://www2.hawaii.edu/~tshea/), and a simple

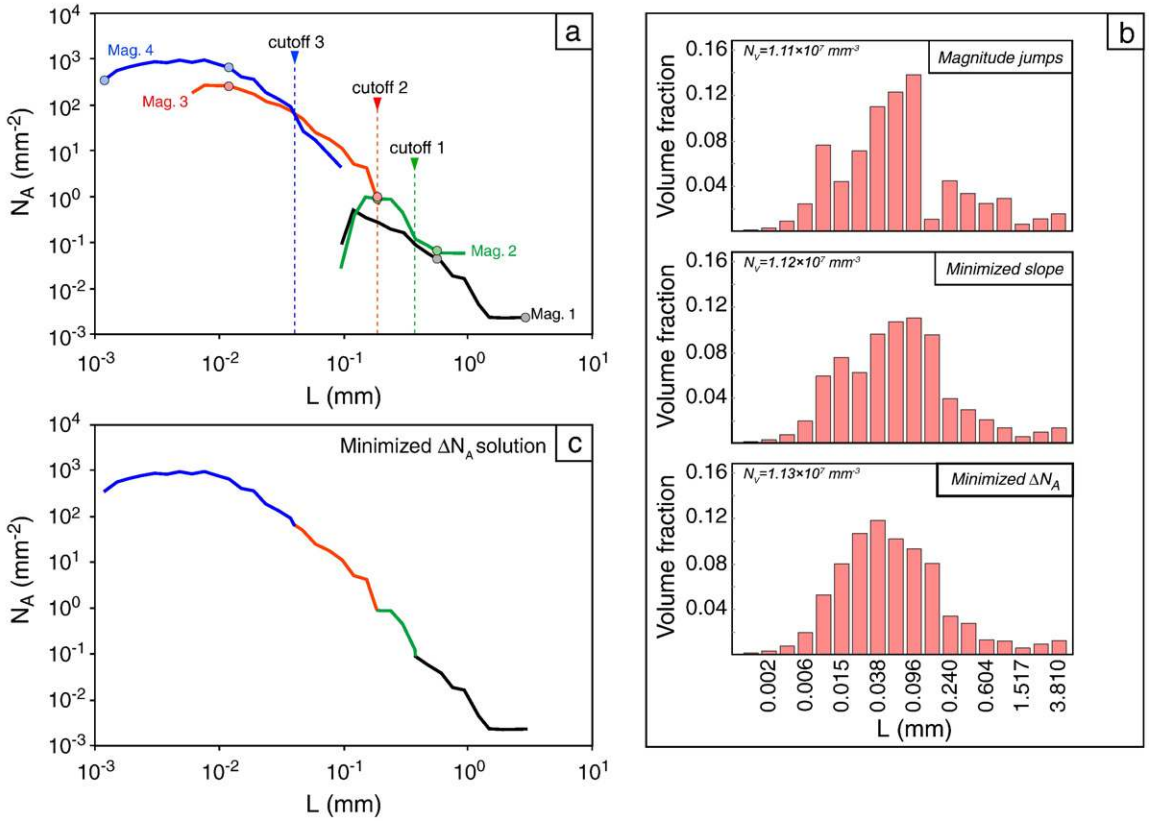

Fig. 7. Illustration of the influence of how magnification cutoffs are chosen within a Vesuvius 79AD pumice. (a) A plot of N_A vs. equivalent diameter L for each magnification (1–4) results in decreasing N_A with increasing L for each decreasing magnification. A certain amount of overlap is required for the FOAMS program (or the operator) to choose the best N_A coverage per size range. (b) Vesicle volume distribution histograms resulting from several magnification cutoff trials; the first cutoff technique tested consisted in arbitrarily choosing boundaries at order of magnitude size changes, the second technique involved minimizing slope differences between the N_A curves of two overlapping magnifications (resulting cutoffs reported as round symbols), and the third method minimized N_A changes (resulting cutoffs reported as dotted lines and arrows). (c) The best result for this pumice clast was obtained using the N_A-minimizing method. Notice that there are still some irregularities in the resulting curve.

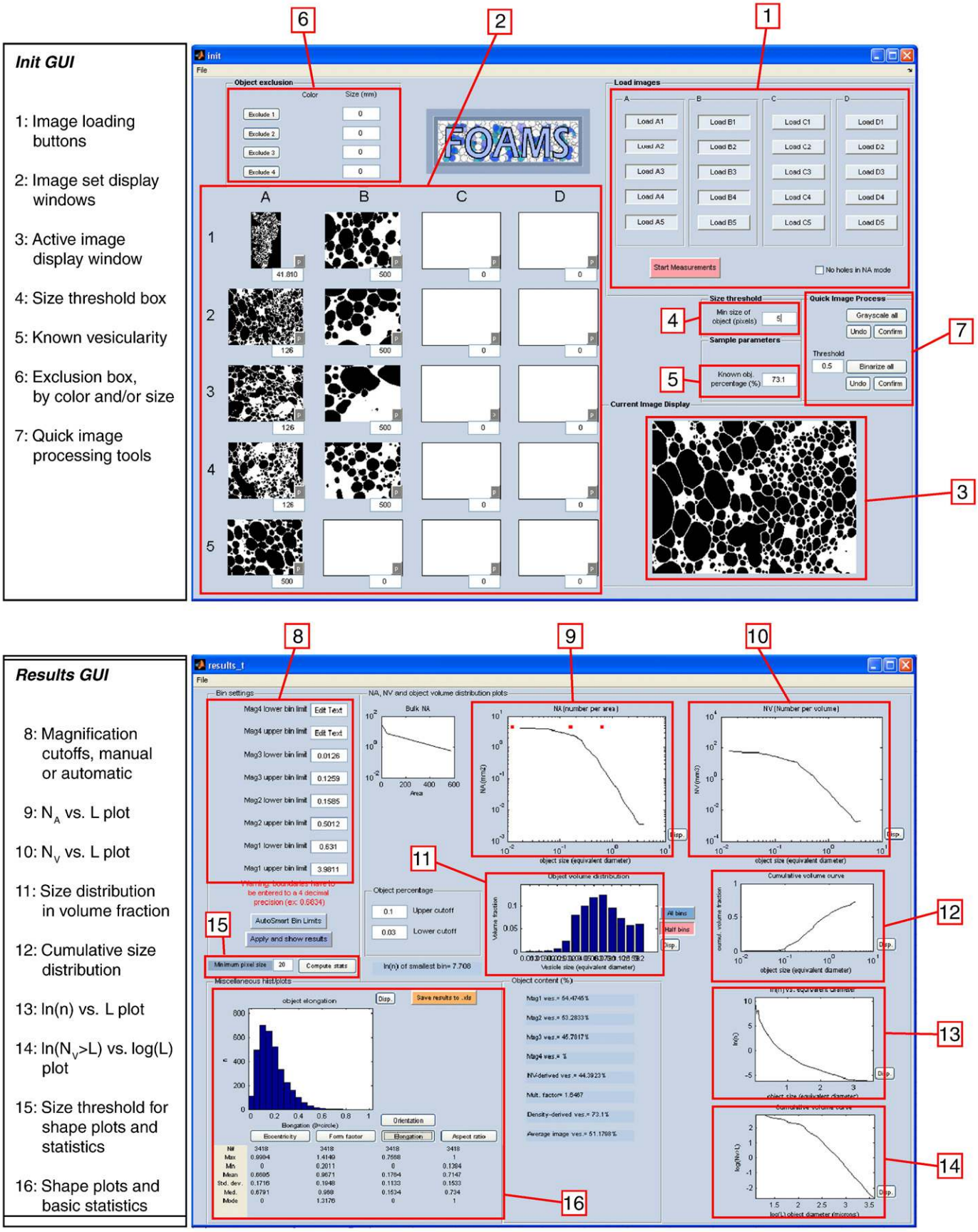

Fig. 8. FOAMS "Init" (top) and "Result" (bottom) user interfaces and graphical contents.

programming flow-chart is given in the additional material. FOAMS uses Matlab™'s image processing toolbox functions and exploits simple user interfaces (GUI) operated using buttons. The function *bwlabel* allows grouping of objects of similar grayscale level if they are each surrounded by another shade of gray, and the function *regionprops* is used to measure object dimensions (area A, equivalent diameter L, perimeter p) and find the best-fit ellipse to acquire other important features (long and short axis, orientation). Edge-bordering vesicles are by definition not surrounded by any medium and are thus discarded from the subsequent measurements. Stereological conversion is applied to number density per unit area (N_A) measurements and results are plotted on a second GUI.

4.2. Modus operandi

A detailed manual is provided with the program, and only a succinct outline is presented here. Once FOAMS is launched, a first GUI ("init") appears (Fig. 8). The user loads anywhere from 1 to 20 grayscale or binary images (number 1 in Fig. 8) all displayed in miniature windows (number 2 in Fig. 8). To allow better visualization, any image can be shown on a larger "active" window (number 3, Fig. 8). Image scales (in pixels per mm) are inserted next to each subwindow, and the minimum diameter (in pixels) that defines the smallest measurable objects is defined by the user (number 4 in Fig. 8). The entered value defines the smallest geometric bin (in diameter units), and each subsequent bin is generated by a simple $10^{0.1}$ multiplication. Because vesicularities derived through stereological conversion may be substantially offset from the density-derived one, the known vesicularity can also be entered (number 5, Fig. 8). Prior to starting measurements, objects that need to be discarded from the analysis (e.g. phenocrysts) can be excluded from the image areas (number 6, Fig. 8) by size or grayscale value. The quick image treatment tools (number 7, Fig. 8) simply converts all images loaded into FOAMS into grayscale or binary images, however, this is useful only when analyzed objects are homogeneous or when only two clearly distinct phases are present (e.g., crystal-free rock).

When all parameters and images are loaded, a second GUI ("results") appears (Fig. 8). A spreadsheet containing N_A vs. L data ("N_A_mag") for each magnification is created and can be used to define better cutoffs. Either FOAMS computes the magnification cutoffs automatically, or the user enters their own (number 8). After stereological conversion, results are plotted within the GUI and new spreadsheets incorporating all measurements as well as some simple 2D shape statistics are created.

4.3. Plots and outputs

FOAMS generates a variety of plots and output files that include:

(1) N_A/N_V vs. L plots (Fig. 8, numbers 9 and 10): raw number density plots are not useful per se for anything more than verification. Since the N_A vs. L plot was constructed from portions of each magnification (e.g. Fig. 7), there is a risk that the transition from one to the next is not smooth and ideal. This plot allows the user to be critical about how well each size range will be represented, and whether or not some anomalies might be expected in distributions due to abrupt step-like transitions.

(2) Vesicle size distributions are plotted in terms of *volume fraction* (VVD, Fig. 8, number 11 and CVVD, Fig. 8, number 12), and *number densities* (VSD, Fig. 8, number 13 and CVSD, Fig. 8, number 14). Because magnification cutoffs transitions may not be completely smooth, some unexpected spikes may appear within VVDs. In order to minimize the amount of such noise within the distribution, the number of bins is typically halved.

(3) Data files: All parameters measured and calculated using FOAMS are produced as spreadsheets (Excel® or Text format) for the user's convenience.

(4) Vesicle shape panel (Fig. 8, number 16): In FOAMS, several shape factors have been implemented including roundness parameters such as aspect ratio $AR = \frac{a}{b}$, as well as a new complexity parameter termed "regularity" $rg = \frac{A}{\pi ab}$), where a and b are best-fit ellipse semi-long and semi-short axes respectively, and A is the vesicle area (see Appendix C for more details).

5. Application to natural volcanic rocks

Three volcanic units have been selected to provide comparative examples of products of very different volcanic eruptions and to illustrate how variations within the application of the suggested methodology can affect resulting texture measurements. These three eruptions differ strongly in their volcanic explosivity indices (VEI) and show large contrasts in vesicle number, size, and distribution. Rather than reiterating existing interpretations for these deposits, we focus on how changes in chosen magnifications, magnification cutoffs, and minimum measured bubble diameter can all modify the outcome of the textural characterization procedure. Nonetheless, for context, we provide a brief summary of their volcanological setting as well as previous vesicularity studies.

5.1. Case studies, density measurements

Samples of lava flow units collected near Makapuu point in Oahu, Hawaii (USA) supply an example of vesicle textures in mostly outgassed basaltic lavas (VEI = 0). At Makapuu, successions of 'a'a, pāhoehoe, and transitional lava flow units were erupted during the formation of the Koolau lava shield, 1.8–2.8 Ma ago (Doell and Dalrymple, 1973). We consider here a transitional unit displaying strong variations in vesicle number, size and arrangement on the scale of a single rock sample (~20 cm long) (Gurioli et al., in preparation). The lower section of the samples collected from this unit possesses textural features typical of pāhoehoe, with numerous round vesicles of fairly similar sizes, whereas the upper portion resembles 'a'a, enclosing mostly irregular vesicles of varying sizes. This variation allows us to investigate the influence of merging measurements from across a heterogeneous sample.

The second study is a sample of scoria clasts collected after a Strombolian eruption (VEI = 1–2) at Villarrica (Chile) in 2004 (Gurioli et al., 2008).

The third case study comprises a collection of samples from the 79AD eruption of Vesuvius from the first Plinian unit (EU2, Cioni et al., 1992) (VEI = 6). These microvesicular clasts are part of an extensive dataset covering part of the 79AD eruptive stratigraphy (Gurioli et al., 2005) and were chosen due to their relatively simple vesiculation history.

All three sample sets were processed using the guidelines described previously to derive density and vesicularity. Several pieces of Makapuu lava collected from 'a'a, pāhoehoe and transitional units were sectioned into smaller subsamples, which were then used for density measurements. Although full textural characterization is presented only for a transitional lava, density measurements for 'a'a and pāhoehoe are also shown in Fig. 9a for comparison. Over 100 clasts of Villarrica scoria and Vesuvius white pumice were used to obtain the density histograms shown in Fig. 9b and c. The average Makapuu transitional lava density is 1780 kg m^{-3}, and modal densities for Villarrica and Vesuvius are 900 kg m^{-3} and 600 kg m^{-3} respectively. Corresponding vesicularities are 38, 66 and 77% respectively. It is worth noting that density histograms can be broadly polymodal (Makapuu and Villarrica) or strongly unimodal (Vesuvius).

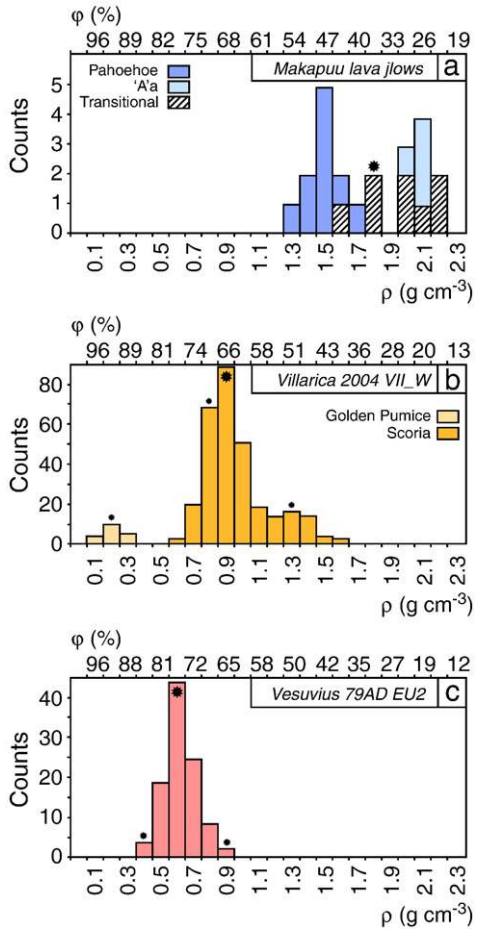

Fig. 9. Density measurements (bottom *x*-axis) and corresponding vesicularities (top *x*-axis) for (a) Makapuu lava flows including three physically distinct units (pāhoehoe, 'a'a, transitional), (b) Villarrica basaltic scoria samples including some very low density samples of golden pumice, and (c) Vesuvius 79AD EU2 pumice samples. Large stars represent chosen samples within all three eruption units and small stars stand for lower and higher density clasts that were also investigated in other contributions (Gurioli et al., 2005, 2008).

5.2. Contrasting imaging strategies

We used different imaging strategies for the three sample types that reflect differences in the vesicle populations. The smallest vesicles in the Makapuu lava are ~0.1 mm and could be studied at a magnification of 25×, while the largest vesicles of ~5 mm required two scan magnifications (slab at 2.5× and thin section at 5×) (Fig. 10a). Measurements of vesicularity, vesicle size, and number distributions were made using the bulk sample (top + bottom) as well as the upper and lower domains individually, to address the issue of heterogeneity within a sample. Thus three magnifications (2.5×, 5×, and 25×) were sufficient to resolve all vesicle sizes; five 25× images within each 5× image allowed sufficient coverage of each textural domain. In contrast, the smallest vesicles (~0.01 mm in diameter) in the Villarrica scoria required a maximum magnification of 100× (Fig. 10b). Thin sections (magnification 5×) were usually big enough to cover the largest enclosed vesicles, (15 mm). Three magnifications (5×, 25×, and 100×) were sufficient to include all vesicles, however, as a nesting strategy we selected three 25× images within the thin section and two 100× within each 25× image (Fig. 10b). This choice was motivated by the fact that vesicles in Villarrica samples span 3 orders of magnitude (0.01–10 mm) and hence that each magnification is equally important to characterize the full textural domain. Finally, highly vesicular white pumice from the 79AD eruption of Vesuvius included vesicles as small as 0.001 mm, while the largest individuals reached around 2–3 mm, thus the vesicle sizes covering a total of 4 orders of magnitude. A magnification of 500× is required to resolve objects as small as 0.001 mm at an error of 5% for one misrepresented pixel (Fig. 2). Four magnifications were consequently used to embody all vesicles (5×, 25×, 100×, and 500×), and nests consisted of two images within each magnification (i.e. IMR of 2:1 for all magnifications; Fig. 10c).

5.3. Influence of magnification

To test the dependence of resulting size distributions and vesicle number densities on the range of magnifications used, FOAMS runs were completed using contrasting levels of nesting. For Makapuu samples, VVDs of the bottom ("pāhoehoe") section of the subsample were calculated using two or three magnifications (2.5×, 5×, and ±25×). Villarrica samples were run using a combination of one to three magnifications from 5× to 100×. Vesuvius EU2 pumice was tested using one to four magnifications (5× to 500×). To include as many vesicles per image as possible, we set the minimum diameter to 5 pixels. Results are shown in Fig. 11. In Makapuu lavas, the distribution represented by 2.5× and 5× magnifications alone (Fig. 11a) clearly lacks the population of small vesicles. For larger bubbles, the distribution is smoother when 25× images are included. The effect of increasing or decreasing the number of magnifications also affects the computed N_V (~20 mm^{-3} instead of ~100 mm^{-3}). In Villarrica samples, (Fig. 11b) the broad shape of the distribution is also present within the first magnification (5×) but the smaller bubbles are missing. This illustrates how additional magnifications (100×) may leave volume distributions relatively unmodified, while strongly increasing number densities (from 1100 to 3200 mm^{-3}). Vesuvius pumice vesicles present an even more extreme case of how apparent number densities increase by orders of magnitude as more small vesicles are added (Fig. 11c). Overall, for all three examples, measurement of accurate number densities requires precise measurement of the smallest vesicles, while accurate measurement of vesicle volume distributions requires precise measurement of the larger vesicles. This does not imply that extremely high magnifications must always be included: while vesicles are better resolved, the area of each image is smaller and thus the risk of capturing non representative portions of a heterogeneous sample significantly increases.

5.4. Influence of minimum diameter on size distributions

Equally important to the choice of nesting strategy and magnifications, the minimum vesicle diameter, measured as number of pixels, strongly shapes the outcome of texture analysis. For each location, runs were made using six minimum diameters from 1 to 20 pixels (equivalent to 1–315 pixels in area), corresponding to uncertainties of 100 to 0.5% for one misrepresented pixel. The obtained N_A vs. L curves for all three samples (note: for Makapuu, only the curve corresponding to the bottom unit is reported) share a similar concave downward form for vesicle sizes greater than about 0.1, 0.01 and 0.001 mm for Makapuu, Villarrica and Vesuvius respectively (Fig. 12). This type of hook-shaped, concave-down curve is expected for processes that generate log-normal distributions, where the number of objects scales inversely with size. The trends become horizontal as the smallest vesicles are reached. Below this size range, trends diverge from smooth to multiple relatively saw-toothed, irregular segments. This change in behavior is a sign that a size threshold has been reached under which measurements become unreliable. The minimum diameter is thus generally chosen above this limit. For Makapuu, Villarrica and Vesuvius respectively, 15, 10 and 5 pixels allow discarding noise data that could alter the results. A preliminary run through the program using a minimum diameter of 1 pixel is therefore useful to see the full spectrum of measurements, from noise to meaningful data.

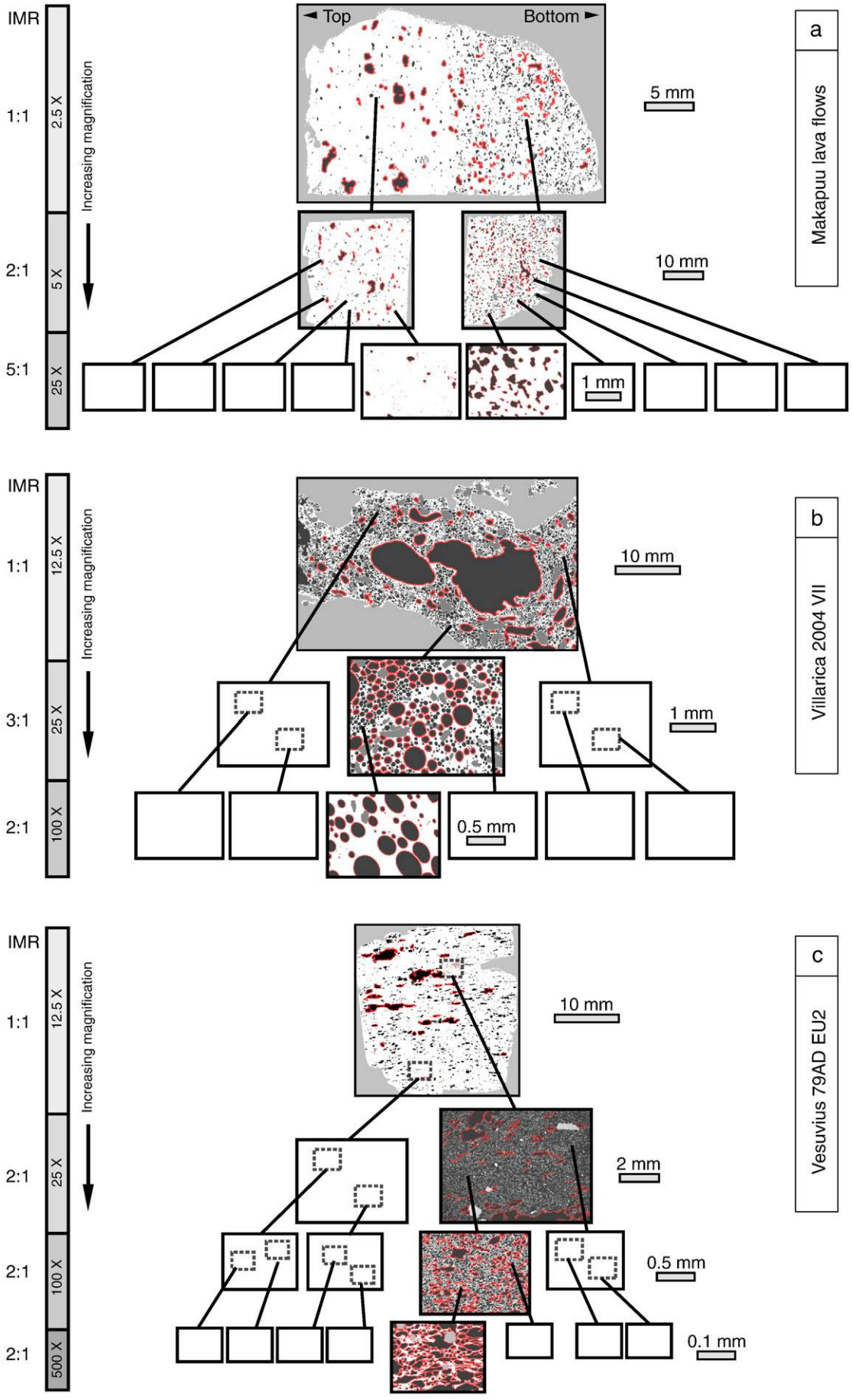
IMR
1:1
2:1
5:1
2.5 X
5 X
25 X
Increasing magnification
◄ Top
Bottom ►
5 mm
10 mm
1 mm
a
Makapuu lava flows
IMR
1:1
3:1
2:1
12.5 X
25 X
100 X
Increasing magnification
10 mm
1 mm
0.5 mm
b
Villarica 2004 VII
IMR
1:1
2:1
2:1
2:1
12.5 X
25 X
100 X
500 X
Increasing magnification
10 mm
2 mm
0.5 mm
0.1 mm
c
Vesuvius 79AD EU2

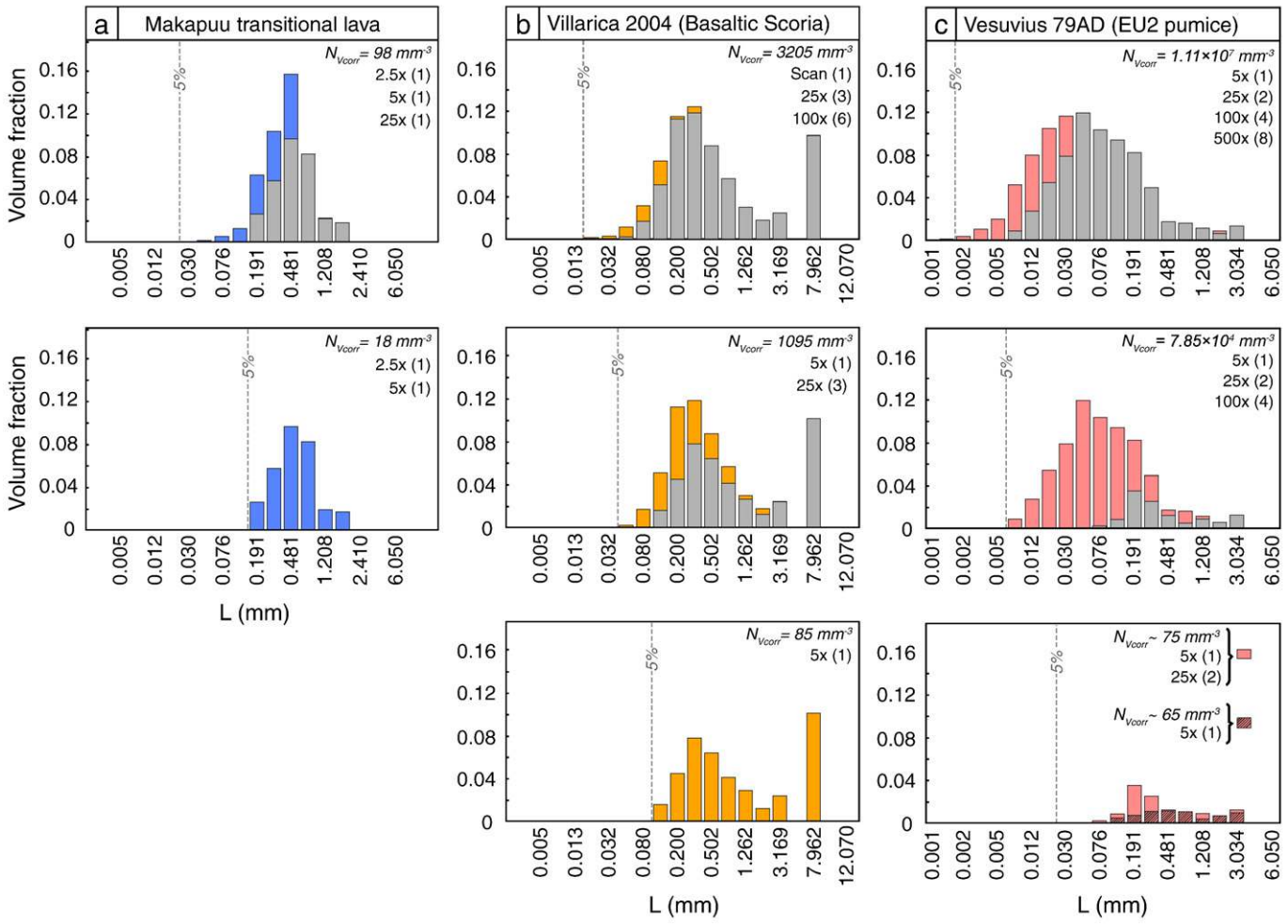

Fig. 11. Influence of adding or discarding images of increasing magnifications for (a) Makapuu lavas (bottom section only), (b) Villarrica scoria, and (c) 79AD Vesuvius EU2 pumice. In each case, the distribution resulting from using only lower magnification imagery is shown in gray. Here, a 5-pixel diameter was used to generate these distributions, thus the lower size limit corresponds to the point under which the uncertainty for each misrepresented pixel is greater than 5%. Vesicle number densities corrected for melt (N_{Vcorr}) calculated for each combination of magnifications are also reported.

Makapuu VVDs (Fig. 13a) illustrate how merging data from regions of contrasting textures may alter the distribution. Distribution in the bulk sample is bimodal at 0.6 and 6 mm (Table 1), but the bottom pāhoehoe-like section shows only one 0.6 mm mode whereas the top ʻāʻa section has two (1.5 mm and 6 mm). Thus, interpretations have to be made after delineation of the two textural domains. On cumulative plots, the lower sample is characterized by a fairly smooth sigmoid curve that could be interpreted as one or two nucleation events, while the upper sample shows a clearer coalescence signature (cf., Fig. 8b). Ln(n) vs. L plots show less direct evidence for this merging process as both curves overlap significantly. Even though the curves reported in the log(N_V>L) vs. log(L) plot are fairly similar, an exponential trend fits the lower sample better, whereas a power-law is more appropriate for the upper section and yields $d = 2.54$ (Table 1). The choice of a 15 pixel minimum diameter appears adequate when looking at the consequences of lowering the boundary (note: the minimum diameter test was only applied to the bottom section). VVDs and CVVDs are unaffected at diameters below 20 pixels, whereas the CVSD curve stabilizes before the 15 pixel limit and increases again at smaller diameters.

The Villarrica sample (Fig. 13b) shows a peculiar VVD with one major mode at 0.04 mm and a secondary, widely separated mode around 8 mm. The latter mode results from the two large vesicles visible on the scanned thin section (Fig. 10b) while the first mode is generated by the bulk of the vesicle population. This bimodality is clearly seen on the cumulative plot as a step-like heterogeneity. On the VSD, within the size range defined by the bulk of the distribution, the trend is curved and shows an inflection around 3 mm. The curve then becomes horizontal as no vesicles are measured from around 2.5 mm to 8 mm. A power-law fit shows $R^2 = 0.97$, with exponent

Fig. 10. Nested imaging strategies chosen for the three studied eruptions. For Makapuu (a), vesicles cover a fairly narrow size range and smaller ones measure in the order of 0.1 mm so that only three relatively low magnifications (25× at maximum) are needed. To cover as much area as possible, ten images are selected for the highest magnification (IMR = 5:1), and one nest is used for each of two distinct textural domains. Villarrica vesicles (b) also cover narrow size intervals and three magnifications are also used. Here, higher magnifications (100×) are required since smaller vesicles are about 0.01 mm in size. Due to ambiguous textural variations, we preferred to select three images within the first nest to better characterize different domains. (c) Vesuvius pumice contains vesicles that span several orders of magnitude in size and four magnifications are preferred. Smallest individuals reach 0.001 mm, hence the largest magnification was chosen to be quite high (500×). In all images, the red outlines depict the vesicles which will actually be measured in each range, after magnification cutoffs are applied.

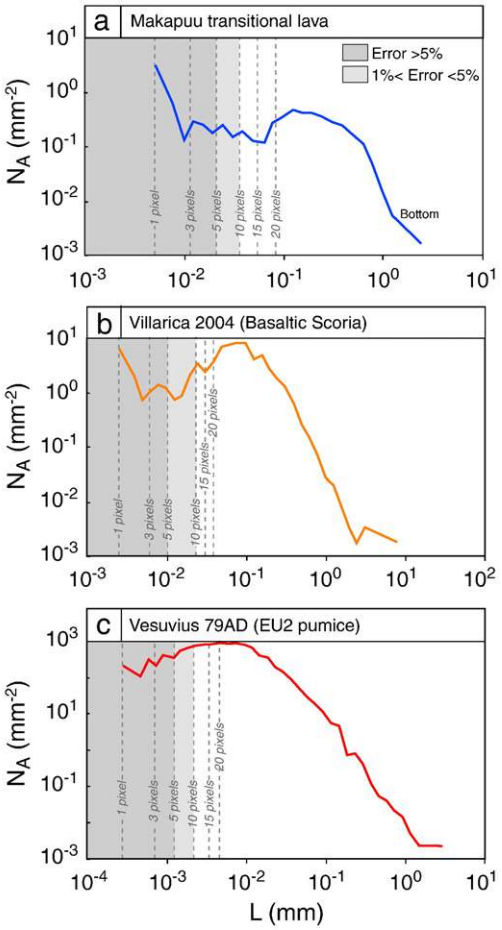

Fig. 12. Vesicle number density per area (N_A) measured in the investigated samples. (a) Makapuu, (b) Villarrica, (c) Vesuvius. Gray dotted lines correspond to the resolution limit allowed by various minimum diameters. Under these boundaries, N_A values used to obtain N_Vs are discarded. Typically, a maximum uncertainty of 5% is allowed. Any vesicle smaller than this is thus considered noise. For Makapuu the best choice of minimum diameter is probably situated around 15–20 pixels, for Villarrica at about 5–10 pixels, and at Vesuvius 5 pixels.

$d = 3.25$, higher than in most basaltic pyroclasts (Blower et al., 2002; Sable et al., 2006; Polacci et al., 2008) and close to those measured in Mt Mazama pumice (Klug et al., 2002). Unlike Makapuu, the chosen minimum diameter becomes more of an issue for Villarrica since selecting values of 15 or 20 pixels diameter leads to discarding a non-negligible portion of the VVD, CVVD and $\log(N_V) > \log(L)$ distributions. Opting for 10 pixels in this case is a better option and preserves important fractions of the distribution.

The Vesuvius 79AD EU2 pumice (Fig. 13c) shows a fairly smooth but weakly bimodal distribution with the major mode around 0.04 mm, and the minor second mode at about 3 mm. This second mode is barely visible on the CVVD plot where the curve is sigmoidal but can be inferred from the slight asymmetry of the two sigmoid tails. The trend on the ln (n) vs. L plot is very smoothly curved with no apparent break. Much like at Villarrica, a power-law fit results in a $R^2 \sim 0.99$ and yields an exponent of approximately 3.5, on the upper range of values found by Klug et al. (2002) in Mt Mazama pumice. Like at Villarrica, Vesuvius pumice VVD, CVVD and CVSD distributions are truncated with respect to the smaller vesicles if the minimum diameter is set too high. To account for the full range of sizes, this diameter needs to be set at around 5 pixels. This choice involves a higher uncertainty (~5% for 1 incorrect pixel) than for larger diameter bubbles. As discussed previously, nonetheless, it is the only way to account for the small vesicle population at the selected maximum magnifications. As suggested earlier, the investigator might consider this uncertainty to be unacceptable and may wish to capture additional sets of images at higher magnifications to improve resolution.

5.5. Number densities

Two number density formulations have appeared throughout this methodology; N_V (or N_{Vcorr}), is obtained by counting vesicles within distinct size classes and summing them, and N_{Vfit} is the total number of vesicles derived from exponential fitting of the VSD (Appendix B) (Table 1). On the latter plots, a single exponential fit is rarely possible and only a portion of the entire curve is usually considered. The N_{Vfit} values reported in Table 1 were obtained by fitting only the smaller size fraction for all considered examples. The initial number density of nuclei n_0 used to compute N_{Vfit} is taken at the smallest measured size and not at zero. N_{Vcorr} as well as N_{Vfit} values were calculated using various minimum diameters (1, 3, 5, 10, 15 and 20 pixels) for all three deposits (Fig. 14, Table 1). A decrease in minimum diameter in all three samples results in drastic increases in vesicle number density. In Makapuu subsamples, N_{Vcorr} decreases from 3000 mm^{-3} to 30 mm^{-3} as minimum diameter increases from 1 to 20 pixels, and Villarrica number density decrease from 1×10^4 mm^{-3} to about 3×10^3 mm^{-3}. On the higher end of the number density spectrum, N_{Vcorr} values measured in Vesuvius 79AD samples decreases by about 10^6 mm^{-3}, from a maximum of 1.6×10^7 mm^{-3} (1 pixel minimum diameter) to a minimum of 3.7×10^6 mm^{-3} (20 pixels diameter). For most tested minimum diameters, N_{Vfit} values track N_{Vcorr} surprisingly well. Discrepancies begin to appear only when very small minimum diameters are reached, and suggest that substantial noise is included in the number density data. Thus, if the minimum diameter is chosen adequately, N_{Vfit} and N_{Vcorr} should approximately coincide.

6. Discussion: precautions and caveats

The vesicle texture characterization methodology presented here provides guidelines for efficient sample processing, from field collection to data representation. While applying these methods minimizes time-requirements while keeping the number of analyzed objects statistically significant, there are several problems that warrant further caution. These problems include the incapacity to characterize adequately elongated vesicles, the operator bias associated with the various choices needed to obtain the data, the small number of large vesicles typically present, and the difficulty of deriving statistics from the distributions.

6.1. The issue of elongated vesicles

Vesicles are often stretched either during transport (e.g. fluidal bombs), or sheared during ascent close to the conduit margins (e.g. long-tube or fibrous pumice, Polacci et al., 2001; Klug et al., 2002; Polacci et al., 2003). Unfortunately, the current version of FOAMS does not transform 2D data adequately for vesicles that have been significantly deformed or sheared. This implies that during sample collection, clasts with very elongated vesicles must be avoided. While it may be argued that this selection might bias the textural characterization of the deposit as a whole, investigating vesicle size and number density in very deformed samples is prone to larger uncertainties associated with textural overprinting: number densities will hardly reflect conduit ascent rates and vesicle sizes will be affected by shearing-induced coalescence. Nonetheless, we acknowledge that implementation of textural quantification parameters for elongate objects is needed for investigations that may focus on the variation of shearing in lava flows or laterally across the conduit through deformation of vesicles; for instance, tube pumice samples cut perpendicular to elongation can provide information relevant to

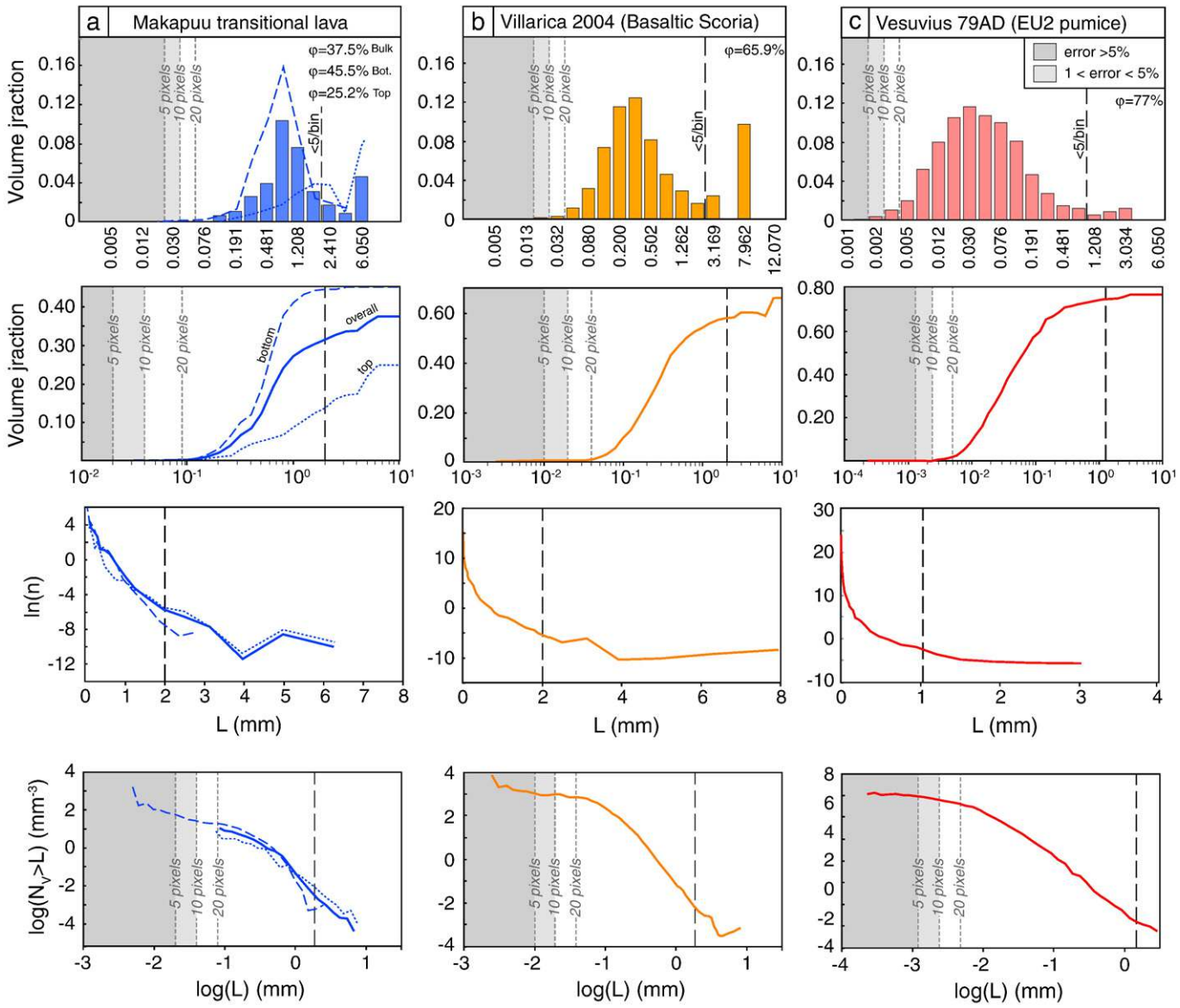

Fig. 13. Vesicle size distributions in terms of volume fraction (VVD), cumulative size distributions (CVVD), size distributions in terms of number density (VSD), and cumulative number density plots (CVSD) for (a) Makapuu transitional lava, (b) Villarrica scoria, and (c) Vesuvius 79AD pumice. Vesicularities are reported in VVD plots. Gray dotted lines represent minimum diameter boundaries; i.e. the limits under which any vesicle smaller than a given diameter in pixels will be discarded. Black dashed lines are limits beyond which bins possess less than 5 vesicles each.

permeability modeling. Measuring size and shape parameters of deformed vesicles within obsidian samples exhibiting low vesicularities has also proven useful to determine strain rate (Rust et al., 2003). Thus, as mentioned previously, the option to select pre-defined shapes with their corresponding intersection probabilities should be available in future versions of FOAMS. This is in part why measurements of shape parameters are already implemented into the program. Despite the problems associated with the assumption of sphericity, the size and number distributions obtained through FOAMS are shown to be reliable; indeed, our case studies (Makapuu, Villarrica, and Vesuvius) were chosen to represent complex real cases and the derived size, number and shape distributions, as well as resulting N_V values are very consistent with qualitative macroscopic observations.

6.2. Larger vesicle populations

In subsamples taken from welded/competent volcanic rocks such as Makapuu lava flows, it is fairly easy to sample a large enough area either by collecting big samples, or by using reconstructive field photography (Polacci and Papale, 1997). In scoria clasts, however, the analyzable area is typically limited to a few square centimeters. The difficulty of analyzing the larger size populations is particularly well illustrated in the case of Villarrica scoria: in all plots, the transition from the first to the second mode is abrupt because the large bubbles (most likely generated by coalescence and post-fragmentation expansion, Gurioli et al., 2008) are not present in the smaller magnification images (Fig. 13b). This is an issue which cannot readily be dealt with. To characterize these populations under robust statistical conditions, a much larger sample would probably be needed, of which at least 10 clasts would be selected for each density mode. Due to time constraints, however, this is harder to achieve. As a result, large vesicle populations in scoria or pumice clasts are typically represented by a few individuals rather than by a statistically significant population (cf. large vesicles in Villarrica and Vesuvius samples, Fig. 10b). Hence, particularly in size distribution plots, it is advisable to determine and display sizes above which the distribution is represented by less than 5–10 individuals per bin (Fig. 13).

Table 1
Summary of main physical and textural parameters in the three samples investigated.

Location	ρ (kg m^{-3}) [a]	ϕ (%)[b]	n[c]	Diameter (pixels)[d]	Mag. (pix m^{-1}) [e]	Min. size (mm)[f]	N_{Vcorr} (mm^{-3})[g]	$n = n_0^{e(-L/G\tau)}$[h]	R^2[i]	$G\tau$ (mm)[j]	N_{Vfit} (mm^{-3}) [k]
Makapuu	1780	45.5	3862	1	252	0.00397	27.03×10^2	$n=(2.23\times10^5)^{e(-203.85L)}$	0.76	0.0049	8.93×10^2
			2209	3	”	0.01190	2.05×10^2	$n=(2.11\times10^4)^{e(-92.05L)}$	0.79	0.0105	1.32×10^2
			1541	5	”	0.01984	0.98×10^2	$n=(3.85\times10^3)^{e(-39.28L)}$	0.83	0.0255	0.82×10^2
			780	10	”	0.03968	0.48×10^2	$n=(5.75\times10^2)^{e(-12.62L)}$	0.85	0.0792	0.51×10^2
			473	15	”	0.05952	0.31×10^2	$n=(1.90\times10^2)^{e(-7.69L)}$	0.86	0.1301	0.29×10^2
			339	20	”	0.07937	0.30×10^2	$n=(4.49\times10^2)^{e(-11.67L)}$	0.92	0.0857	0.28×10^2
Villarica	900	65.9	7181	1	500	0.00200	21.19×10^3	$n=(1.25\times10^5)^{e(-41.00L)}$	0.44	0.0244	8.23×10^3
			5998	3	”	0.00600	4.32×10^3	$n=(6.36\times10^4)^{e(-35.71L)}$	0.53	0.0280	4.22×10^3
			4867	5	”	0.01000	3.20×10^3	$n=(2.05\times10^4)^{e(-18.06L)}$	0.64	0.0554	2.78×10^3
			2883	10	”	0.02000	2.69×10^3	$n=(2.05\times10^4)^{e(-17.28L)}$	0.93	0.0579	2.46×10^3
			1742	15	”	0.03000	2.27×10^3	$n=(1.94\times10^4)^{e(-16.71L)}$	0.96	0.0598	2.06×10^3
			1095	20	”	0.04000	1.93×10^3	$n=(1.98\times10^4)^{e(-17.18L)}$	0.95	0.0582	1.70×10^3
Vesuvius	600	77	11214	1	4150	0.00024	1.59×10^7	$n=(3.87\times10^9)^{e(-637.94L)}$	0.65	0.0016	2.26×10^7
			10009	3	”	0.00072	1.56×10^7	$n=(2.43\times10^9)^{e(-477.31L)}$	0.89	0.0021	1.57×10^7
			8313	5	”	0.00120	1.13×10^7	$n=(1.88\times10^9)^{e(-448.28L)}$	0.97	0.0022	1.06×10^7
			5322	10	”	0.00241	0.76×10^7	$n=(1.57\times10^9)^{e(-385.31L)}$	0.94	0.0026	0.70×10^7
			3627	15	”	0.00361	0.50×10^7	$n=(8.89\times10^8)^{e(-285.78L)}$	0.99	0.0035	0.48×10^7
			2662	20	”	0.00482	0.37×10^7	$n=(8.81\times10^8)^{e(-284.97L)}$	0.98	0.0035	0.34×10^7

[a] Density, as measured using Houghton and Wilson (1989).
[b] Vesicularity, derived from density.
[c] Number of vesicles measured.
[d] Minimum diameter used as input to define the smallest measurable vesicle.
[e] Maximum magnification used for each case study.
[f] Minimum vesicle size analyzed as defined by (column d/column e).
[g] Vesicle number density (N_{Vcorr}) per volume melt.
[h] Exponential best-fit equation as measured from VSD plots; n_0 is initial number of nuclei and L is diameter.
[i] Least squares goodness of fit.
[j] Values of growth rate (G) times vesiculation timescale (τ) derived from column h.
[k] Vesicle number density (N_{Vfit}) derived from (column $j\times n_0$).

6.3. Minimum detectable object and statistics

We showed that the choice of the minimum number of pixels necessary to adequately represent a vesicle is crucial since it has a large influence on measured estimates of N_V. For small increases in minimum resolvable diameter, number density can drop by an order of magnitude. This decrease was observed to be stronger with increasing explosivity: each 5 pixel increase in the input threshold diameter resulted in about 5, 15, and 30% decreases in N_{Vcorr} for Makapuu, Villarrica and Vesuvius samples respectively. Thus, to obtain accurate measurements of N_{Vcorr}, it is crucial to select minimum diameters that ensure that the measured vesicles are above “noise” level. Uncertainties within N_{Vcorr} will then mostly depend on the accuracy of vesicularity measurements used to calculate number density per melt volume. The errors associated with misrepresentation (addition or omission) of 1 or several pixels during acquisition and image rectification will thereafter solely influence the precision at which small vesicle sizes are measured. On a VVD plot, such errors will not strongly modify the shape of the distribution particularly towards smaller bins.

Another issue inherent to the acquisition of results through binning and stereological conversion to 3D is that individual data are inevitably lost in the process. This means that statistical analysis of the data will have to be done directly on distribution curves with no real decision on how large the bins are and how many objects they typically contain. Even so, distribution fitting is still possible using geometric binning, as it appears that most distributions fall within the logarithmic family (log-normal, Weibull, logistic and exponential, Proussevitch et al., 2007a). Because few distributions are normal, we recommend avoiding the use of the mean and using modes instead. The actual “log-normal” mean can still be obtained through the normal mean and standard deviation derived from the geometrically binned distribution.

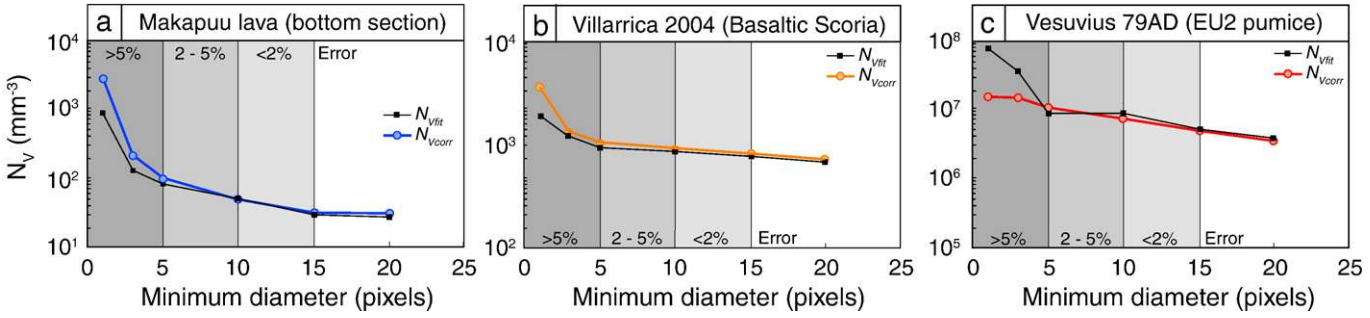

Fig. 14. Influence of minimum measured vesicle size (in pixels per diameter) on the calculated N_{Vcorr} for (a) Makapuu lavas, (b) Villarrica scoria, and (c) Vesuvius white pumice. In all cases the obtained number densities are extremely dependent on the choice of the smallest resolvable vesicle size (in pixels). Number densities obtained using VSD fitted curves (N_{Vfit}) are also shown as black squares. Notice the general disagreement between the two values for samples containing a high density of vesicles (Villarrica and Vesuvius) and the good concordance with Makapuu lavas. Zones filled with increasing gray shades report errors associated with misrepresentation of 1 pixel.

7. Conclusions

With increasing interest in the study of vesicles in volcanic rocks, there is a need for a standardized methodology that captures and quantifies the parameters essential to understanding magma ascent and degassing. By adopting a generalized procedure for textural characterization, comparisons of vesicle size distributions, number densities and shapes between eruptions become possible, and operator errors are minimized. We emphasized the need to find a certain balance between the total number of images captured and processed, and time-requirements. Different nested imaging configurations are needed in the case of natural samples collected for different eruption styles. In nested imaging configurations, the number of images required to fully characterize most samples falls typically below 20. The textural characterization algorithm FOAMS can measure and analyze objects within these images in just seconds. Current limitations arise from lacking elongate conversion factors, which may introduce some bias in the situations where bubbles have extreme shapes. On the other hand, strengths of this methodology include the possibility of informed decision-making in all steps of the textural investigation process, while keeping time-consuming phases to a minimum. Because the entire technique from thin section to the quantification stage is based on multiscale imagery, it allows for virtually infinite vesicle resolutions, even at micrometer scale, as long as a statistically viable area is imaged. Future steps include implementing stereological solutions for ellipsoids are into upcoming versions of FOAMS, as well as achieving comparisons between XRCMT and Stereology(FOAMS)-derived distributions.

Acknowledgments

The authors wish to acknowledge NSF grants EAR 0409303, 0537950, 0537543, 0537459 and 0739060 and the New Zealand Marsden Fund. This methodology greatly benefited from discussions with Thomas Giachetti and Tim Druitt. We thank Wendy Stovall, Ian Schipper and Natalie Yakos for (very patiently!) providing much needed validation for FOAMS. Thoughtful reviews from Laura Pioli and Sharon Allen were greatly appreciated.

Appendix A. Summary of stereological conversion equations relevant to FOAMS taken from Sahagian and Proussevitch (1998)

N_{V1} and subsequent number densities can be expressed by a generalized equation of form:

$$N_{Vi} = \frac{1}{P_i \overline{H}_i'} \times \left(N_{Ai} - \sum_{j=1}^{i-1} P_{j+1} \overline{H}_{j+1}' N_{V(i-j)} \right) \quad (A.1)$$

(Sahagian and Proussevitch, 1998)

N_A is measured number density per unit area (mm^{-2}) for size ranges 1 to i , P the probability of intersecting particles of the same size ranges (1 to i), and $\overline{H}_i'$ the mean projected height.

To avoid several stages of computations, Sahagian and Proussevitch (1998) rewrite Eq. (A.1) as:

$$N_{Vi} = \frac{1}{\overline{H}_i'} \times \left(\alpha_i N_{Ai} - \sum_{j=1}^{i-1} \alpha_{j+1} N_{A(i-j)} \right) \quad (A.2)$$

where conversion coefficients

$$\alpha_i = \frac{1}{P_1} \left(\alpha_1 P_i - \sum_{j=1}^{i-2} \alpha_{j+1} P_{i-j} \right) \quad (A.3)$$

For spherical particles, the probability of intersecting objects through a specific size is written:

$$P(r_1<r<r_2) = \frac{1}{R}\left(\sqrt{R^2 - r_1^2} - \sqrt{R^2 - r_2^2} \right) \quad (A.4)$$

R is the sphere radius, r is the cross-section radius, and r_1 and r_2 are the lower and upper limits of the particular size ranges considered.

Appendix B. Vesicle size distributions

Theoretical background behind VSDs

In theory, assuming that nucleation and growth rates are constant throughout the vesiculation process, numerous physical parameters can be derived from segments of VSD curves. These include nucleation rates (J), growth rates (G), number of initial nuclei (n_0), the total number of vesicles per unit volume (N_{Vfit}) and the characteristic bubble diameter (L).

These parameters are found using the steady-state conservative exponential equation:

$$n = n_0 \exp\left(\frac{-L}{G\tau}\right) \quad (B.1)$$

Then nucleation rates (J, $mm^{-3}\,s^{-1}$) are simply:

$$J = n_0 G \quad (B.2)$$

In theory, if the data are linear on an $\ln(n)$ vs. L plot, the total number density of vesicles per volume melt can be retrieved through the zeroth moment of Eq. (B.2) (Cashman and Mangan, 1994):

$$N_{Vfit} = n_0 G\tau \quad (B.3)$$

In turn, the first moment gives the dominant diameter:

$$L_{fit} = G\tau \quad (B.4)$$

The value of N_{Vfit} can be compared subsequently to the N_V directly measured within the sample to test whether the trend adequately represents the actual data. If they are similar, then the fit can be considered robust.

Theoretical background behind log(N_V)>log(L) plots

Numerical models by Blower et al. (2002) demonstrate that in log (N_V>L) vs. log(L) plots, one to three nucleation events are able to generate exponential curves (Fig. 8d), of form:

$$\log(N_V > L) \propto e^{-L} \quad (B.5)$$

whereas numerous nucleation events or continuous nucleation and growth produce power-law linear trends:

$$\log(N_V > L) \propto L^{-d} \quad (B.6)$$

where d is the power-law exponent.

This type of plot was used to differentiate between exponential and power-law distributions, and between single, multiple or continuous nucleation (Gaonac'h et al., 1996a,b; Blower et al., 2001, 2002; Gaonac'h et al., 2005; Polacci et al., 2008).

Power-law fitted distributions are usually only valid for a certain size range (Blower et al., 2002), and are seemingly applicable to most volcanic rocks as they represent multiple or continuous nucleation events. Gaonac'h et al. (1996a,b, 2005) predicted that

a single value of exponent $d \sim 2.5$, close to the value anticipated for Apollonian packing (Blower et al., 2001), could apply to most vesicular samples, from lava flows to pumice. In the literature, however, varying d exponents have been found: $d = 2.5$ in Basaltic scoria from Izu Oshima subplinian eruption (Blower et al., 2002), 2.8 within Stromboli basaltic scoria (Bai et al., 2008; Polacci et al., 2008; Note that their form of Eq. (B.6) expresses measurements as volume instead of radius), 2.8 in Etnean basaltic scoria (Simakin et al., 1999), 2.7–2.9 in Plinian basaltic scoria (Sable et al., 2006), 3.3 in rhyodacitic pumice (Klug et al., 2002), and 3.9 in dacitic pumice (Adams et al., 2006). Thus, on the whole, it seems this exponent increases with increasing eruption explosivity, an outcome forecasted by numerical models (Blower et al., 2001).

In contrast, exponential fitted distributions are applied in $\log(N_V > L)$ vs. $\log(L)$ plots when the trend is nearly horizontal towards smaller class sizes and curves down towards larger objects. These fits do not seem to apply to many situations, however, and are thought to represent cases in which one or only few nucleation events have occurred (Blower et al., 2002; Bai et al., 2008). Coalescence tends to produce curves looking fairly similar to exponential trends, with the distinction nonetheless that a more horizontal tail may exist towards large size classes (Polacci et al., 2008; Bai et al., 2008). In turn, collapse textures may produce a curve which rapidly decreases towards low N_V values and quickly becomes near-horizontal as largest sizes are approached.

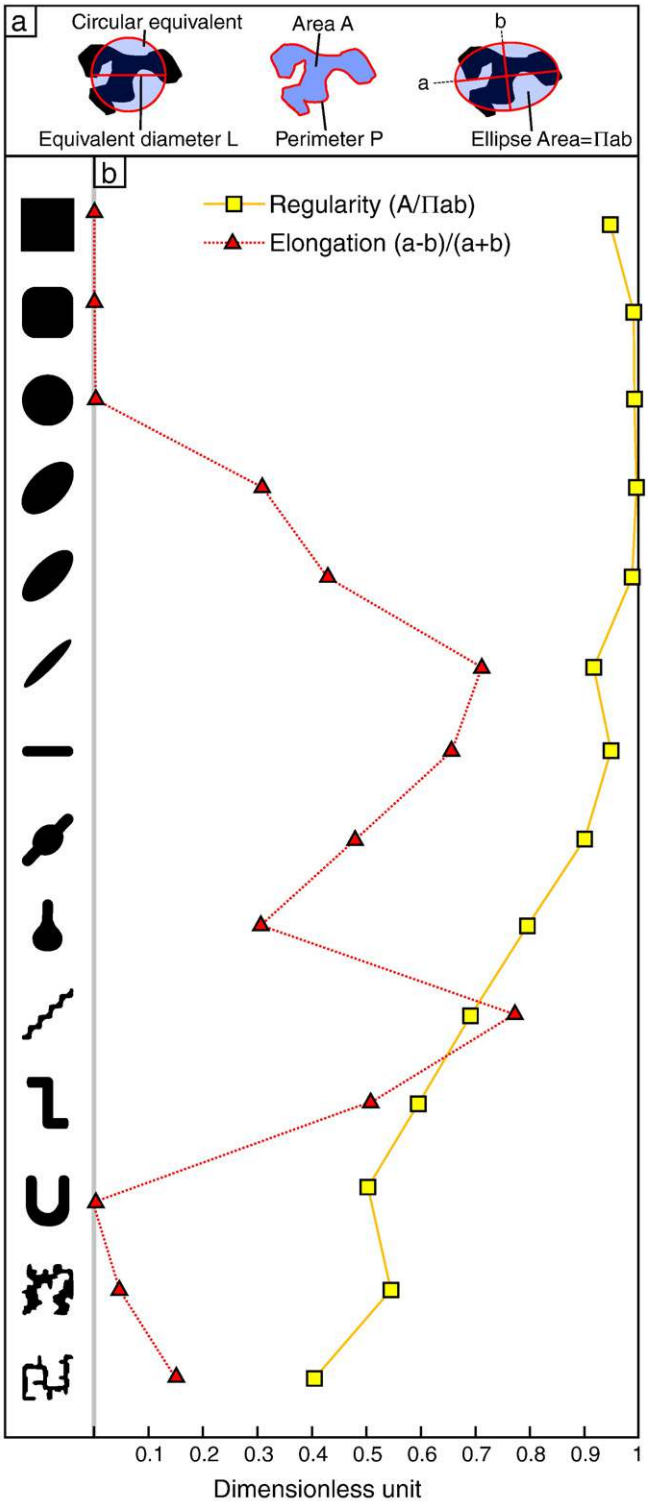

Fig. C1.

Appendix C. Shape parameters

More often, the problems of shape are addressed using sphericity parameters and much less often consider complexity or both. Polacci and Papale (1997) and Rust et al. (2003) have used what is typically referred to as aspect ratio $AR = \frac{b}{a}$ where a is best-fit ellipse semi-long axis and b is semi-short axis. Circular objects possess aspect ratios of 1 while extremely stretched objects tend towards zero, however, the inverse of AR is sometimes used, where the larger the value, the more the object has an elongated form. Manga et al. (1998), Polacci et al. (2001), Rust et al. (2003) and Mongrain et al. (2008) used elongation $\varepsilon = \frac{a-b}{a+b}$, a fairly similar parameter for which values of 0 represent circular objects and values of 1 extremely elongated ones. Aspect ratio and elongation are equally adequate to characterize vesicle deformation and both are available as outputs in FOAMS. Vesicle complexity has been dealt with using the shape factor $SF = \frac{4\pi A}{p^2}$, where A is vesicle Area and p is perimeter (Orsi et al., 1992; Cashman and Mangan, 1994). In this case, a perfect circle has SF = 1, and more complex shapes will have SF tending towards 0. Because the latter ratio also varies somewhat with object elongation, it is however difficult to distinguish which of the two geometrical variations (i.e. elongation vs. complexity) is more influential. Therefore, we introduce the "regularity" parameter as the ratio of the area (A, mm^2) to the area of the corresponding best-fit ellipse $rg = \frac{A}{\pi ab}$. This formulation has the advantage of accounting for irregularities in vesicle outline while disregarding elongation. All measured dimensions are shown in Fig. C1. To ensure the capability of elongation/aspect ratio and regularity to fully characterize vesicle shape, we ran a series of tests involving shapes of decreasing circularity and increasing complexity using binary objects of up to 300 pixels. Elongation increases along with object stretching, and, as expected, behaves more chaotically when comparing shape complexities (Fig. C1). Regularity stays constant for varying elongations and regularly decreases with increasing complexity.

References

Adams, N.K., Houghton, B.F., Fagents, S.A., Hildreth, W., 2006. The transition from explosive to effusive eruptive regime: the example of the 1912 Novarupta eruption, Alaska. Geol. Soc. Am. Bull. 118, 620–634. doi:10.1130/B25768.1.

Allen, S.R., 2005. Complex spatter- and pumice-rich pyroclastic deposits from and andesitic caldera-forming eruption: the Siwi pyroclastic sequence, Tanna, Vanuatu. Bull. Volcanol. 67, 27–41.

Bai, L., Baker, D.R., Rivers, M., 2008. Experimental study of bubble growth in Stromboli basalt melts at 1 atm. Earth Planet. Sci. Lett. 267, 533–547. doi:10.1016/j.epsl.2007.11.063.

Blower, J.D., Keating, J.P., Mader, H.M., Phillips, J.C., 2001. Inferring volcanic degassing processes from vesicle size distributions. Geophys. Res. Lett. 28, 347–350. doi:10.1029/2000GL012188.

Blower, J.D., Keating, J.P., Mader, H.M., Phillips, J.C., 2002. The evolution of bubble size distributions in volcanic eruptions. J. Volcanol. Geotherm. Res. 120, 1–23.

Blundy, J., Cashman, K.V., 2008. Petrologic reconstruction of magmatic system variables and processes. Rev. Mineral. & Geochem. 69, 179–239.

Burgisser, A., Gardner, J.E., 2005. Experimental constraints on degassing and permeability in volcanic conduit flow. Bull. Volc. 67, 42–56.

Carey, R.J., Houghton, B.F., Thordarson, T., 2008. Contrasting styles of welding observed in the proximal Askja eruption deposits I: regional welding. J. Volcanol. Geotherm. Res. 171, 1–19. doi:10.1016/j.jvolgeores.2007.11.020.
Cashman, K.V., Mangan, M.T., 1994. Physical aspects of magmatic degassing II: constraints on vesiculation processes from textural studies of eruptive products. In: Carroll, M. (Ed.), Volatiles in Magmas. Min. Soc. Am, Washington, D. C, pp. 447–478.
Cashman, K.V., Mangan, M.T., Newman, S., 1994. Surface degassing and modifications to vesicle size distributions in active basalt flows. J. Volcanol. Geotherm. Res. 62, 45–68.
Cigolini, C., Laiolo, M., Bertolino, S., 2008. Probing Stromboli volcano from the mantle to paroxysmal eruptions. In: Annen, C., Zellmer, G.F. (Eds.), Dynamics of Crustal Magma Transfer, Storage and Differentiation. : Special Publications, vol. 304. Geological Society, London, pp. 33–70.
Cioni, R., Marianelli, P., Sbrana, A., 1992. Dynamics of the AD 79 eruption: stratigraphic, sedimentological and geochemical data on the successions from the Somma–Vesuvius southern and eastern sectors. Acta Vulcanol. 2, 109–123.
Cluzel, N., Laporte, D., Provost, A., Kannewischer, I., 2008. Kinetics of heterogeneous bubble nucleation in rhyolitic melts: implications for the number density of bubbles in volcanic conduits and for pumice textures. Contrib. Mineral. Perol. 156, 745–763.
Degruyter, W., Bachmann, O., Burgisser, A., 2010. Controls on magma permeability in the volcanic conduit during the climactic phase of the Kos Plateau Tuff eruption (Aegean Arc). Bull. Volcanol. 72, 63–74.
Doell, R.R., Dalrymple, G.B., 1973. Potassium–argon ages and paleomagnetism of the Waianae and Koolau Volcanic Series, Oahu, Hawaii. Geol. Soc. Am. Bull. 84, 1217–1241.
Gaonac'h, H., Lovejoy, S., Stix, J., Scherzter, D., 1996a. A scaling growth model for bubbles in basaltic lava flows. Earth Planet. Sci. Lett. 139, 395–409.
Gaonac'h, H., Stix, J., Lovejoy, S., 1996b. Scaling effects on vesicle shape, size and heterogeneity of lavas from Mount Etna. J. Volc. Geotherm. Res. 74, 131–153.
Gaonac'h, H., Lovejoy, S., Schertzer, D., 2005. Scaling vesicle distributions and volcanic eruptions. Bull. Volcanol. 67, 350–357.
Gualda, G.A.R., Rivers, M., 2006. Quantitative 3D petrography using X-ray tomography: application to Bishop Tuff pumice clasts. J. Volcanol. Geothem. Res. 154, 48–62.
Gurioli, L., Houghton, B.F., Cashman, K.V., Cioni, R., 2005. Complex changes in eruption dynamics during the 79AD eruption of Vesuvius. Bull. Volcanol. 67, 144–159.
Gurioli, L., Harris, A.J.L., Houghton, B.F., Polacci, M., Ripepe, M., 2008. Textural and geophysical characterization of explosive basaltic activity at Villarrica volcano. J. Geophys. Res. 113, B08206. doi:10.1029/2007JB005328.
Higgins, M.D., 2000. Measurement of crystal size distributions. Am. Mineral. 85, 1105–1116.
Hon, K., Kauahikaua, J., Denlinger, R., Mackay, K., 1994. Emplacement and inflation of pāhoehoe sheet flows: observations and measurements of active lava flows on Kilauea Volcano, Hawaii. Geol. Soc. Am. Bull. 106, 351–370.
Houghton, B.F., Wilson, C.J.N., 1989. A vesicularity index for pyroclastic deposits. Bull. Volcanol. 51, 451–462.
Ketcham, R.A., 2005. Computational methods for quantitative analysis of three-dimensional features in geological specimens. Geosphere 1, 32–41.
Ketcham, R.A., Carlson, W.D., 2001. Acquisition, optimization and interpretation of X-ray computed tomographic imagery: applications to the geosciences. Comput. Geosci. 27, 381–400.
Klug, C., Cashman, K.V., 1994. Vesiculation of May 18, 1980, Mount St. Helens magma. Geology 22, 468–472.
Klug, C., Cashman, K.V., Bacon, C., 2002. Structure and physical characteristics of pumice from the climactic eruption of Mount Mazama (Crater Lake), Oregon. Bull. Volcanol. 64, 486–501.
Lautze, N.C., Houghton, B.F., 2007. Linking variable explosion style and magma textures during 2002 at Stromboli volcano, Italy. Bull. Volcanol. 69, 445–460.
Lensky, N.G., Navon, O., Lyakhovsky, V., 2004. Bubble growth during decompression of magma: experimental and theoretical investigation. J. Volcanol. Geotherm. Res. 129, 7–22.
Lyakhovsky, V., Hurwitz, S., Navon, O., 1996. Bubble growth in rhyolitic melts: experimental and numerical investigation. Bull. Volcanol. 58, 19–32.
Manga, M., Castro, J., Cashman, K.V., 1998. Rheology of bubble bearing magmas. J. Volcanol. Geotherm. Res. 87, 15–28.
Mangan, M.T., Cashman, K.V., 1996. The structure of basaltic scoria and reticulite and inferences for vesiculation, foam formation, and fragmentation in lava fountains. J. Volcanol. Geotherm. Res. 73, 1–18.
Mangan, M., Sisson, T., 2000. Delayed, disequilibrium degassing in rhyolite magma: decompression experiments and implications for explosive volcanism. Earth Planet. Sci. Lett. 183, 441–455.
Marsh, B.D., 1988. Crystal size distribution (CSD) in rocks and the kinetics and dynamics of crystallization: I. Theory. Contrib. Mineral. Petrol. 99, 277–291.
Marsh, B.D., 1998. On the interpretation of crystal size distributions in magmatic systems. J. Petrol. 39, 553–600.
Mastrolorenzo, G., Pappalardo, L., 2006. Magma degassing and crystallization processes during eruptions of high-risk Neapolitan-volcanoes: evidence of common equilibrium rising processes in alkaline magmas. Earth Planet. Sci. Lett. 250, 164–181.
Mock, A., Jerram, D.A., 2005. Crystal size distributions (CSD) in three dimensions: insights from the 3D reconstruction of a highly porphyritic rhyolite. J. Petrol. 46, 1525–1541.
Mongrain, J., Larsen, J.F., King, P.L., 2008. Rapid water exsolution, degassing, and bubble collapse observed experimentally in K-phonolite melts. J. Volcanol. Geotherm. Res. 173, 178–184.
Morgan, D.J., Jerram, D.A., 2006. On estimating crystal shape for crystal size distribution analysis. J. Volcanol. Geotherm. Res. 154, 1–7.
Mourtada-Bonnefoi, C.C., Laporte, D., 2002. Homogeneous bubble nucleation in rhyoliticmagmas: an experimental study of the effect of H2O andCO2. J. Geophys. Res. 107, B4. doi:10.1029/2001JB00290.
Mourtada-Bonnefoi, C.C., Laporte, D., 2004. Kinetics of bubble nucleation in a rhyolitic melt: an experimental study of the effect of ascent rate. Earth Planet. Sci. Lett. 218, 521–537.
Namiki, A., Manga, M., 2006. Influence of decompression rate on the expansion velocity and expansion style of bubbly fluids. J. Geophys. Res. 111, B11208. doi:10.1029/2005JB004132.
Noguchi, S., Toramaru, A., Shimano, T., 2006. Crystallization of microlites and degassing during ascent: Constraints on the mechanical behavior of magma during the Tenjo Eruption on Kozu Island, Japan. Bull. Volcanol. 68, 432–449.
Okumura, S., Nakamura, M., Tsuchiyama, A., 2006. Shear-induced bubble coalescence in rhyolitic melts with low vesicularity. Geophys. Res. Lett. 33, L20316. doi:10.1029/2006GL027347.
Okumura, S., Nakamura, M., Tsuchiyama, A., Nakano, T., Uesugi, K., 2008. Evolution of bubble microstructure in sheared rhyolite: formation of a channel-like bubble network. J. Geophys. Res. 113, B07208.
Orsi, G., Gallo, G., Heiken, G., Wohletz, K., Yu, E., Bonani, G., 1992. A comprehensive study of pumice formation and dispersal: the Cretaio tephra of Ischia (Italy). J. Volcanol. Geotherm. Res. 53, 329–354. doi:10.1016/03770273(92)90090-Z.
Papale, P., Neri, A., Macedonio, G., 1998. The role of magma composition and water content in explosive eruptions. 1. Conduit dynamics. J. Volcanol. Geotherm. Res 87, 75–93.
Piochi, M., Mastrolorenzo, G., Pappalardo, L., 2005. Magma ascent and eruptive processes from textural and compositional features of Monte Nuovo pyroclastic products, Campi Flegrei, Italy. Bull.Volcanol. 67, 663–678.
Pioli, L., Pistolesi, M., Rosi, M., 2007. Pumice textures as an indicator of magma mingling and fragmentation processes at Stromboli volcano (Italy). Eos Trans. AGU, 88(52), Fall meet. Suppl., Abstract V22A-02.
Polacci, M., Papale, P., 1997. The evolution of lava flows from ephemeral vents at Mount Etna: insights from vesicle distribution and morphological studies. J. Volcanol. Geotherm. Res. 76, 1–17.
Polacci, M., Papale, P., Rosi, M., 2001. Textural heterogeneities in pumices from the climactic eruption of Mount Pinatubo, 15 June 1991, and implication for magma ascent dynamics. Bull. Volcanol. 63, 83–97.
Polacci, M., Pioli, L., Rosi, M., 2003. The Plinian phase of the Campanian Ignimbrite eruption (Phlegrean Fields, Italy): evidence from density measurements and textural characterization of pumice. Bull. Volcanol. 65, 418–432. doi:10.1007/s00445-002-0268-4.
Polacci, M., Baker, D.R., Mancini, L., Tromba, G., Zanini, F., 2006. Three-dimensional investigation of volcanic textures by X-ray microtomography and implications for conduit processes. Geophys. Res. Lett. 33, L13312.
Polacci, M., Baker, D.R., Bai, L., Mancini, L., 2008. Large vesicles record pathways of degassing at basaltic volcanoes. Bull. Volcanol. 70, 1023–1029. doi:10.1007/s00445-007-0184-8.
Polacci, M., Baker, D.R., Mancini, L., Favretto, S., Hill, R.J., 2009. Vesiculation in magmas from Stromboli and implications for normal Strombolian activity and paroxysmal explosions in basaltic systems. J. Geophys. Res. 114, B01206. doi:10.1029/2008JB005672.
Proussevitch, A.A., Sahagian, D.L., 1996. Dynamics of coupled diffusive and decompressive bubble growth in magmatic systems. J. Geophys. Res. 101, 17447–17455.
Proussevitch, A., Ketcham, R.A., Carlson, W.D., Sahagian, D., 1998. Preliminary results of X-ray CT analysis of Hawaiian vesicular basalts. Eos 79 (17), 360.
Proussevitch, A.A., Sahagian, D.L., Tsentalovich, E.P., 2007a. Statistical analysis of bubble and crystal size distributions: formulations and procedures. J. Volcanol. Geotherm. Res. 164, 95–111. doi:10.1016/j.jvolgeores.2007.04.007.
Proussevitch, A.A., Sahagian, D.L., Carlson, W.D., 2007b. Statistical analysis of bubble and crystal size distributions: application to Colorado Plateau basalts. J. Volcanol. Geotherm. Res. 164, 112–126. doi:10.1016/j.jvolgeores.2007.04.006.
Rust, A.C., Cashman, K.V., 2004. Permeability of vesicular silicic magma: inertial and hysteresis effects. Earth Planet. Sci. Lett. 228, 93–107.
Rust, A.C., Manga, M., Cashman, K.V., 2003. Determining flow type, shear rate and shear stress in magmas from bubble shapes and orientations. J. Volcanol. Geotherm. Res. 122, 111–132.
Sable, J.E., Houghton, B.F., Wilson, C.J.N., Carey, R.J., 2006. Complex proximal sedimentation from Plinian plumes: the example of Tarawera 1886. Bull. Volcanol. 69, 89–103.
Sahagian, D.L., Proussevitch, A.A., 1998. 3D particle size distributions from 2D observations: stereology for natural applications. J. Volcanol. Geother. Res. 84, 173–196.
Saltikov, S.A., 1967. The determination of the size distribution of particles in an opaque material from a measurement of the size distribution of their sections. In: Elias, H. (Ed.), Stereology. Springer-Verlag, NY, pp. 163–173.
Shin, H., Lindquist, W.B., Sahagian, D.L., Song, S.R., 2005. Analysis of the vesicular structure of basalt. Comput. Geosci. 31, 473–487.
Simakin, A.G., Armienti, P., Epel'baum, M.B., 1999. Coupled degassing and crystallization: experimental study at continous pressure drop, with application to volcanic bombs. Bull. Volcanol. 61, 275–287.
Song, S.R., Jones, K.W., Lindquist, W.B., Dowd, B.A., Sahagian, D.L., 2001. Synchrotron X-ray computed microtomography: studies on vesiculated basaltic rock. Bull. Volcanol. 63, 252–263.
Sparks, R.S.J., 1978. The dynamics of bubble formation and growth in magmas: a review and analysis. J. Volcanol. Geotherm. Res. 3, 1–37.
Toramaru, A., 1990. Measurement of bubble size distributions in vesiculated rocks with implications for quantitative estimation of eruption processes. J. Volcanol. Geotherm. Res. 43, 71–90.
Toramaru, A., 1995. Numerical study of nucleation and growth of bubbles in viscous magmas. J. Geophys. Res. 100, 1913–1931.
Toramaru, A., 2006. BND (bubble number density) decompression rate meter for explosive volcanic eruptions. J. Volcanol. Geotherm. Res. 154, 303–316.
Underwood, E.E., 1970. Quantitative stereology. Addison-Wesley, Reading. 274 pp.
Wright, H.M.N., Roberts, J.J., Cashman, K.V., 2006. Permeability of anisotropic tube pumice: model calculations and measurements. Geophys. Res. Lett. 33, L17316.
Wright, H.M.N., Cashman, K.V., Rosi, M., Cioni, R., 2007. Breadcrust bombs as indicators of Vulcanian eruption dynamics at Guagua Pichincha, Ecuador. Bull. Volcanol. 69, 281–300.